BOREAS An international journal of Quaternary research

Lateglacial and Holocene sedimentary dynamics in northwestern Baffin Bay as recorded in sediment cores from Cape Norton Shaw Inlet (Nunavut, Canada)

NATHAN STEVENARD, JEAN-CARLOS MONTERO-SERRANO, FRÉDÉRIQUE EYNAUD, GUILLAUME ST-ONGE, SÉBASTIEN ZARAGOSI AND LUKE COPLAND

BOREAS

Stevenard, N., Montero-Serrano, J.-C., Eynaud, F., St-Onge, G., Zaragosi, S. & Copland, L. 2022 (July): Lateglacial and Holocene sedimentary dynamics in northwestern Baffin Bay as recorded in sediment cores from Cape Norton Shaw Inlet (Nunavut, Canada). *Boreas*, Vol. 51, pp. 532–552. https://doi.org/10.1111/bor.12575. ISSN 0300-9483.

The physical, sedimentological, mineralogical and elemental geochemical properties of sediment cores AMD1803-02BC and 01PC from the Cape Norton Shaw Inlet were investigated to reconstruct glacial sediment discharges from southeastern Manson Icefield and document the impact of ice–ocean interactions on the sediment dynamics and opening of the North Water Polynya (NOW) in northwestern Baffin Bay since the last deglaciation. Laminated glaciomarine sediments rich in quartz and feldspar are observed prior to 11 cal. ka BP and were probably deposited by hyperpycnal currents triggered by the local retreat of the southern margin of the Innuitian Ice. Detrital proxies suggest that Early Holocene sediment dynamics were mainly influenced by sea ice and iceberg rafting and meltwater discharges related to the deglaciation of eastern Smith (~11 to 10.65 cal. ka BP) and Jones (~10.7 cal. ka BP) sounds. This also provides an upper limit to the timing of formation of the NOW. The high detrital carbonate contents during 8.8 to 6.6 cal. ka BP confirm that enhanced carbonate-rich sediment export from Nares Strait to northern Baffin Bay occurred during and after the deglaciation of Kennedy Channel (8.8 to 8.2 cal. ka BP). Canadian Shield sediment inputs have dominated since 6.6 cal. ka BP, indicating that sedimentation is mainly influenced by Cape Norton Shaw glacier discharges. The lower level of sedimentation recorded in core 01PC during the Middle to Late Holocene suggests an accelerated landward retreat of the Cape Norton Shaw glaciers in response to warmer marine conditions. During the Neoglacial period, higher sedimentation rates and detrital proxies in the cores suggest increased glacial erosional processes, probably associated with the long-term declines in boreal summer insolation and glacier growth. Finally, mineralogical and grain-size data in core 02BC support the idea that increased Arctic atmospheric temperatures have had an important influence on the glacial dynamics during the industrial period.

Nathan Stevenard (nathan.stevenard@lsce.ipsl.fr), Laboratoire des Sciences du Climat et de l'Environnement/Institut Pierre Simon Laplace, CEA-CNRS-UVSQ, Université Paris-Saclay, Orme des Merisiers, 91191 Gif-sur-Yvette, France; Jean-Carlos Montero-Serrano and Guillaume St-Onge, Institut des sciences de la mer de Rimouski, Université du Québec à Rimouski, Québec-Océan and Geotop, 310 allée des Ursulines, Rimouski, QC, G5L 3A1, Canada; Frédérique Eynaud, Sébastien Zaragosi and Nathan Stevenard, Université de Bordeaux, CNRS, EPOC, EPHE, UMR 5805, Allée Geoffroy Saint-Hilaire, 33615 Pessac, France; Luke Copland, Department of Geography, Environment and Geomatics, University of Ottawa, Ottawa, Ontario K1N 6N5, Canada; *received 30th April 2021, accepted 13th November 2021.*

The North Water Polynya (NOW), located in the northern part of Baffin Bay, is one of the largest and most productive regions in the Arctic. This area is strongly influenced by a mix of warm Atlantic-sourced and cold Arctic waters (Zweng & Münchow 2006; Rykova *et al.* 2015; Jackson *et al.* 2021), glacial discharges from outlet glaciers of the Canadian Arctic Archipelago (CAA) and NW Greenland margin (e.g. Ó Cofaigh *et al.*. 2013; Dowdeswell *et al.* 2015), and drift ice transported via Nares Strait, Jones Sound and Lancaster Sound (Tang *et al.* 2004). The NOW area is highly vulnerable to long-term changes in climate and ocean dynamics (e.g. Tremblay 2002; Mudie *et al.* 2006; Cormier *et al.* 2016; Ribeiro *et al.* 2021; Koerner *et al.* 2021). Indeed, increases in the northward advection of warm Atlantic-sourced water via the West Greenland Current (WGC) and atmospheric temperature can contribute to enhanced mass loss from the glaciers and ice caps of northern Baffin Bay and the NW Greenland margin (e.g. Chauché *et al.* 2014; Cook *et al.* 2019; Wagner *et al.* 2019).

The CAA is composed of Axel Heiberg, Ellesmere and Devon Islands, which carry 25% of the total Arctic terrestrial ice outside of Greenland (Van Wychen *et al.* 2014; Fig. 1A). Based on field observations, Blake (1981) and Curley *et al.* (2021) suggest that glaciers on southern Ellesmere Island attained their respective maximum advances in the late 1800s or early 1900s, and had retreated slightly from this position by the 1980s. Previous studies based on satellite data have highlighted major changes in volume, mass and ice discharge from CAA glaciers and ice caps owing to modern global warming (Van Wychen *et al.* 2014, 2016, 2020; Millan *et al.* 2017; Mortimer & Sharp 2018; Cook *et al.* 2019; Ciracì *et al.* 2020). For example, the mass loss of glaciers in the Queen Elizabeth Islands averaged 17 ± 5 cm a^{-1} water equivalent over the period 1991–2014 (Millan *et al.* 2017) and glacier mass losses in the CAA were the greatest of any region in the world over the period 2003–2019 (Ciracì *et al.* 2020). Coupled atmosphere–snow regional climate models predict that

DOI 10.1111/bor.12575

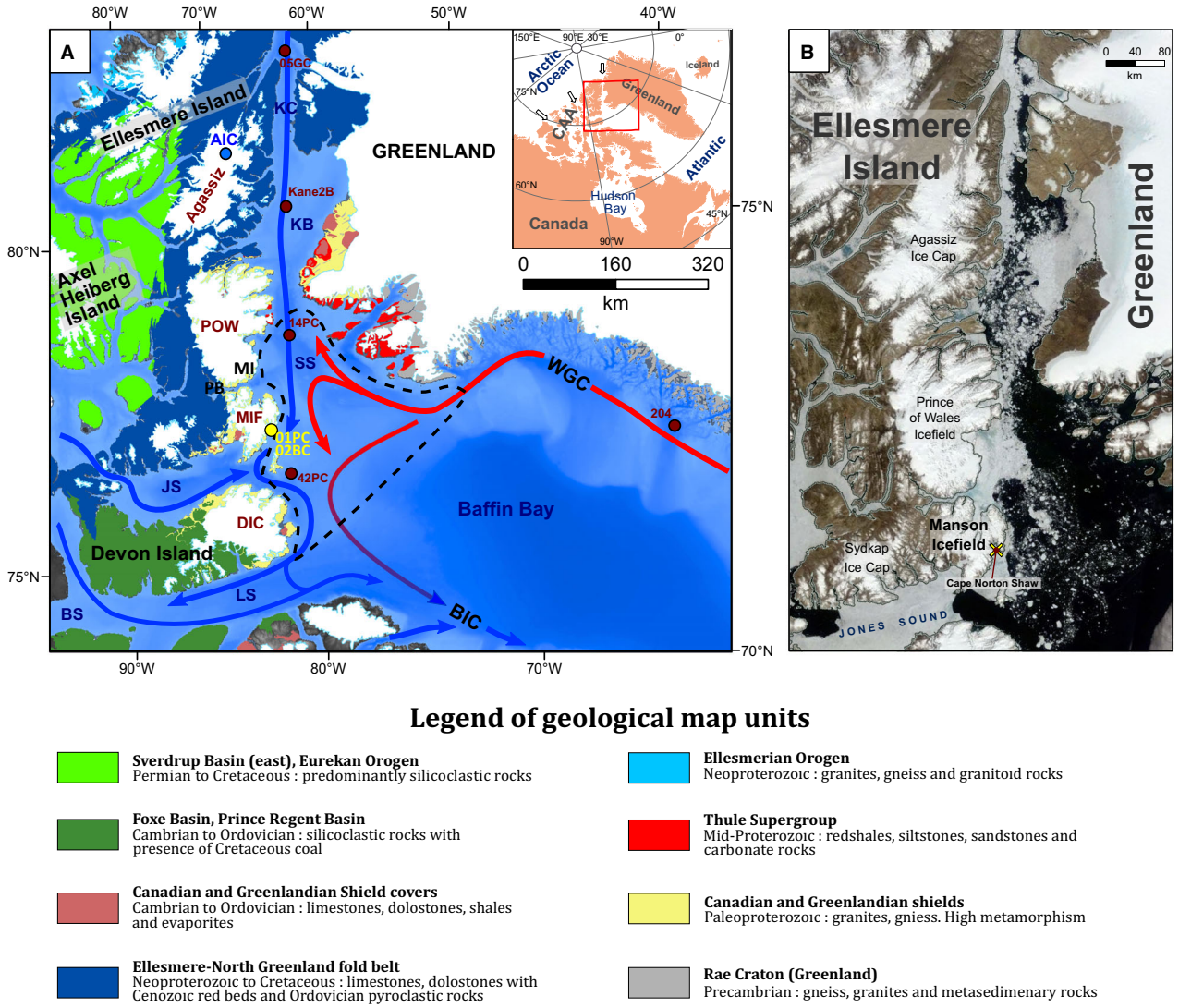

Legend of geological map units

Sverdrup Basin (east), Eurekan Orogen
Permian to Cretaceous : predominantly silicoclastic rocks

Ellesmerian Orogen
Neoproterozoic : granites, gneiss and granitoid rocks

Foxe Basin, Prince Regent Basin
Cambrian to Ordovician : silicoclastic rocks with presence of Cretaceous coal

Thule Supergroup
Mid-Proterozoic : redshales, siltstones, sandstones and carbonate rocks

Canadian and Greenlandian Shield covers
Cambrian to Ordovician : limestones, dolostones, shales and evaporites

Canadian and Greenlandian shields
Paleoproterozoic : granites, gniess. High metamorphism

Ellesmere-North Greenland fold belt
Neoproterozoic to Cretaceous : limestones, dolostones with Cenozoic red beds and Ordovician pyroclastic rocks

Rae Craton (Greenland)
Precambrian : gneiss, granites and metasedimenary rocks

Fig. 1. Maps of study area. A. Topobathymetric and geological map of northern Baffin Bay with major surface currents. Red arrows represent warm surface currents (>2 °C), and blue arrows represent cold Arctic Surface Water (ASW) (<−1 °C). The black dashed line represents the NOW area. WGC = West Greenland Current; BIC = Baffin Island Current; LS = Lancaster Sound; BS = Barrow Strait; JS = Jones Sound; SS = Smith Sound; KB = Kane Basin; KC = Kennedy Channel; HB = Hall Basin; MI = Makinson Inlet; PB = Piliravijuk Bay; MIF = Manson Icefield; POW = Prince of Wales Icefield; DIC = Devon Ice Cap; AIC = Agassiz Ice Cap. Cores studied or cited in this paper are marked by circles: yellow for 01PC = AMD1803-01PC and AMD1803-02BC (this study); red for 14PC = 2001LSSL-014PC (Jennings *et al.* 2019); 204 = AMD14-204 (Caron *et al.* 2019, 2020); Kane2B = AMD14-Kane2B (Caron *et al.* 2020); 05GC = HLY03-05GC (Jennings *et al.* 2011); 42PC = HU2008-029-042PC (St-Onge & St-Onge 2013). B. MODIS satellite image from 2 July 2019 showing a snapshot of the sea ice and iceberg distribution around Jones Sound and Nares Strait (source: NASA Worldview) with the location of cores 02BC and 01PC (yellow cross).

CAA glaciers could lose ~18% of their volume by the end of the 21st century, thus contributing an increase of 0.35 ± 0.24 mm a^{-1} to global sea level rise (Lenaerts *et al.* 2013; Noël *et al.* 2018). However, the response of CAA glaciers to modern global warming is not equally distributed spatially, with the highest retreat rates on small ice masses (Thomson *et al.* 2011; Sharp *et al.* 2014; White & Copland 2018). Furthermore, the long-term (>50 years) calving rates and sediment fluxes of CAA marine-terminating glaciers are poorly documented (e.g. over the whole Holocene; Solomina *et al.* 2015) and little is known about the precise mechanisms (atmospheric or ocean) controlling the frontal changes of these glaciers (Cook *et al.* 2019). Therefore, the long-term glacial sediment dynamics and the role of atmospheric and oceanic forcing on marine-terminating glaciers in the CAA need to be better understood to accurately predict future glacier behaviour and to improve sea level projections (Hodson *et al.* 2013). Glacier-proximal sedimentary sequences can be used to reconstruct past glacier variations and their responses to climate and oceanographic drivers during the Holocene, against which recent changes can be compared.

In the southeastern part of Ellesmere Island, Manson Icefield lies adjacent to northern Baffin Bay and the NOW (Fig. 1). This icefield is characterized by two major marine-terminating glaciers: Jakeman Glacier in the SW and Mittie Glacier in the north (Van Wychen *et al.* 2016, 2020). The icefield contains a large number of surge-type glaciers (Copland *et al.* 2003) and Sharp *et al.* (2014) reported an area loss for southern Ellesmere glaciers, including Manson Icefield, of 5.9% over the period ~1960 to ~2000. Similarly, Cook *et al.* (2019) highlighted the strong retreat of marine terminating glaciers in this region (5–10% loss of glacier length) over the period 1958–2015.

This study focuses on two sediment cores (box core AMD1803-02BC and piston core AMD1803-01PC, hereafter referred to as 02BC and 01PC, respectively), collected in the Cape Norton Shaw Inlet in northwestern Baffin Bay. This inlet provides a good location to record glacial sediment discharges from the southeastern Manson Icefield and the oceanic influences from the WGC and Arctic Surface Water (ASW), as well as the evolution of the NOW. Radiocarbon dating and physical, sedimentological, mineralogical and elemental geochemical properties were combined in these sediment cores to reconstruct past Cape Norton Shaw glacier behaviour and associated environmental drivers for the Holocene. Specifically, these results are integrated to: (i) reconstruct changes in detrital sediment provenance and transport in northwestern Baffin Bay related to climate variability since the last deglaciation; (ii) document the sensitivity of the southeastern part of the Manson Icefield to changing climatic and oceanic conditions during the Holocene; and (iii) assess the significance of recent glaciological changes in the Cape Norton Shaw glaciers. As a whole, our study expands on previous studies in the area (e.g. St-Onge & St-Onge 2014; Georgiadis *et al.* 2018; Jennings *et al.* 2019; Caron *et al.* 2020; Ribeiro *et al.* 2021; Koerner *et al.* 2021) by adopting a multiproxy approach (physical properties, thin sections, grain size, quantitative mineralogy, pXRF) to provide an improved quantification of the sediment provenance and transport pathways in northwestern Baffin Bay since the last deglaciation, and their connection to regional climate history. This study provides more information about the long-term development of the NOW, which is the largest and most productive polynya in the northern hemisphere on which local communities depend (e.g. Ribeiro *et al.* 2021).

Regional setting

Oceanic circulation

The NOW is a major oceanographic corridor for the export of Arctic freshwater to Baffin Bay. Approximately 25% of the total export of ASW to the North Atlantic occurs via Nares Strait, Jones Sound and Lancaster Sound (Fig. 1A; Aagaard & Carmack 1989). Variations in the export of this Arctic freshwater can affect the Atlantic Meridional Overturning Circulation by changing the deep-water convection in the Labrador Sea (Dickson *et al.* 2007) and therefore the global climate (Holland *et al.* 2001; Tang *et al.* 2004; Curry & Mauritzen, 2005). The NOW is influenced by two main currents, the Baffin Island Current (BIC) and the WGC. While the BIC flows southward in the western part of Baffin Bay and originates from cold ASW, the WGC flows northward along the coast of west Greenland before mixing with the BIC in Smith Sound (Fig. 1A; Tang *et al.* 2004). The WGC carries mixed warm and salty Atlantic-sourced Irminger Current water and cold-temperature and low-salinity waters of the East Greenland Current (Tang *et al.* 2004). In the Jones Sound area, the upper waters come mostly from the Pacific and are similar to those flowing in Nares Strait (Fig. 1A; Jones *et al.* 2003).

Surrounding geology and sedimentation

The geological bedrock of northwestern Baffin Bay is complex and dominated by Palaeoproterozoic crystalline rocks that constitute the Canadian and Greenland Shields (Fig. 1A). In the north, the coasts of Smith Sound are dominated by basic volcanic rocks with siliciclastic red beds, which constitute the Thule Supergroup rocks, cropping out on the Greenland coast and the eastern Prince of Wales Icefield (Harrison *et al.* 2011). These red beds can be found within Smith Sound in deep marine sediments (St-Onge & St-Onge 2014; Caron *et al.* 2019; Jennings *et al.* 2019) and can thus be interpreted as a chronostratigraphic marker for the deglaciation of the eastern part of Smith Sound. On southeastern Ellesmere Island and to the east of Devon Island, rocks of the Canadian Shield are predominantly composed of highly metamorphosed granitic or gneissic Precambrian rocks (Harrison *et al.* 2011). To the SW of Jones Sound, the geological units of the Foxe Basin are composed of Cambrian to Devonian siliciclastic rocks rich in dolostones and evaporites (Harrison *et al.* 2011). The Ellesmere–north Greenland fold belt (NW of Jones Sound) is composed of the same types of rocks as the previous geological group but also includes red clay beds and Ordovician volcaniclastic rocks (Harrison *et al.* 2011). Based on existing glacio-geological studies, the area is thought to have undergone an isostatic adjustment of 110–140 m since the Last Glacial Maximum (LGM; 20 cal. ka BP; Blake 1992; Dyke 1998; England *et al.* 2006).

The modern sedimentary dynamics in eastern Manson Icefield area are dominated by inputs from glacial erosion of the surrounding land masses, including the southeastern part of Ellesmere Island and northwestern Greenland (Fig. 1B). Several glacial sedimentary processes, such as iceberg and sea-ice rafting, glaciogenic debris flows, meltwater plumes and turbidity currents,

influence marine sedimentation in this area (e.g. Ó Cofaigh *et al*. 2013; Andrews *et al*. 2018; Andrews 2019; Jennings *et al*. 2019; Caron *et al*. 2020). Most surficial seabed sediments around Manson Icefield are composed of till, silts with high quartz and feldspar contents and clays with high illite, biotite and chlorite contents (Andrews & Eberl 2011; Andrews *et al*. 2018; Andrews 2019). Deglacial and Holocene sedimentation rates near the Manson Icefield area range from 0.67 to 0.046 cm a^{-1} (e.g. Rochon & Vernal 1994; Mudie *et al*. 2006; Bailey *et al*. 2013; St-Onge & St-Onge 2014; Cormier *et al*. 2016; Ribeiro *et al*. 2021).

Deglacial–Holocene history in northern Baffin Bay and Nares Strait

During the LGM and at the beginning of the Early Holocene (11.7 to 10.3 cal. ka BP; Jennings *et al*. 2011, 2019), the export of Arctic freshwater into Baffin Bay was completely blocked owing to the confluence of the Innuitian Ice Sheet (IIS) and the Laurentide Ice Sheet with the Greenland Ice Sheet in Nares Strait, Jones Sound and Lancaster Sound (Dyke *et al*. 2002; England *et al*. 2006; Stokes *et al*. 2015). For example, Blake *et al*. (1996) suggested an ice thickness of 1100 m in Smith Sound during the LGM. The IIS drained the southern part of Ellesmere Island and the northern part of Devon Island and provided detrital material to Jones Sound (England *et al*. 2006).

Several studies conducted in marine basins of the CAA have highlighted the different phases of ice retreat and corridor opening between the Arctic Ocean and Baffin Bay during the last deglaciation. The deglaciation sequences of Lancaster Sound and Barrow Strait are described by Furze *et al*. (2017) and Pieńkowski *et al*. (2012, 2013), and their openings began at 13.2 and 11.5 cal. ka BP, respectively. In Nares Strait, the opening of Smith Sound also occurred during the period from 11.15 to 10.4 cal. ka BP and stabilized with seasonal sea-ice cover between 10.4 and 9.3 cal. ka BP (Jennings *et al*. 2019). Georgiadis *et al*. (2018) and Caron *et al*. (2019, 2020) highlighted the opening of Kane Basin at 9.0 cal. ka BP, at the same time as the opening of Hall Basin (Jennings *et al*. 2011). The Kennedy Channel was the last part of Nares Strait to open up, marking the separation of the IIS and Greenland Ice Sheet at 8.5 to 8.3 cal. ka BP (Jennings *et al*. 2011, 2019; Georgiadis *et al*. 2018), creating a permanent corridor permitting the transport of ASW to Baffin Bay. However, few studies document the deglaciation history of the Jones Sound area and the response of the glaciers around this basin to the establishment of the Arctic–Atlantic throughflow (e.g. Dyke 1998; Dyke *et al*. 1999; England *et al*. 2006; Dalton, 2020). Thus, this study provides an opportunity to fill this knowledge gap and better document glacier responses to palaeoenvironmental changes occurring in this area since the last deglaciation.

Material and methods

Core samples

Box core 02BC (water depth, 124 m; location, 76°28.501′N, 78°44.257′W) and piston core 01PC (water depth, 119 m; location, 76°29.355′N, 78°43.501′W) were collected in the Cape Norton Shaw Inlet, southeastern Manson Icefield, onboard the Canadian Coast Guard Ship (CCGS) icebreaker *Amundsen* during the 2018 ArcticNet expedition (Fig. 1). The determination of coring sites was based on high-resolution seismic profiles and multibeam-bathymetry data (Montero-Serrano *et al*. 2018). Core 02BC is 26-cm long, whereas core 01PC is 198 cm-long. Subsampling was performed on 1-cm-wide sections taken at 4–5-cm intervals for core 01PC (total of 40 samples) and at every centimetre for core 02BC (a total of 26 samples). In core 01PC, a U-channel was collected at the base of the core (124–198 cm; laminated interval) to indurate sediments and obtain thin sections.

Analytical procedures

The detailed methodologies used for the analyses of physical and chemical properties, grain size, quantitative bulk mineralogy and thin sections are presented in Data S1. Briefly, physical properties (including X-ray computed tomography or X-CT, high-resolution photographs, wet bulk densities, low-field volumetric magnetic susceptibilities or k_{LF} and spectral reflectances) and chemical (portable X-ray fluorescence or pXRF) measurements were performed at 1-cm intervals using a GEOTEK Multi-Sensor Core Logger. Sediment grain-size analyses (<2 mm fraction) were performed using a Malvern Mastersizer 2000 laser diffraction grain-size analyser. In addition, discrete sediment samples were dried, weighed, wet sieved at 63 μm, dried, dry sieved at 125 and 400 μm and weighed again to obtain the different sand fractions in weight per cent (wt.%). Gravel-sized clast abundance was determined using the method described by Grobe (1987), which consists of counting the >2 mm fraction on the X-CT scan images of the core in contiguous 2-cm windows. The abundances of coarse sand (>400 μm) and gravel-sized clasts are used here to identify intervals in the cores influenced by the high rafting of coarse material by ice (e.g. ice-rafted debris or IRD and sea-ice transport; Andrews 2000). The sortable silt mean size ($\overline{SS}$) flow speed proxy, which corresponds to the mean grain size of the non-cohesive silt fraction (10–63 μm) and the percentage of sortable silt (*SS*%) in the <63 μm fraction (McCave *et al*. 1995) was calculated for both cores using the approach developed by McCave & Andrews (2019a). Thin sections for the 124–198 cm interval of core 01PC were prepared following the protocol described in Zaragosi *et al*. (2006). Quantitative X-ray diffraction mineralogy (qXRD) of the <2 mm

sediment fraction was studied using the method developed by Eberl (2003) and used in other Quaternary glacial marine studies that address sediment mineralogy in the Arctic (e.g. Andrews & Eberl 2011; Andrews *et al.* 2018; Deschamps *et al.* 2018; Andrews, 2019; Caron *et al.* 2020). The principal minerals that were analysed by this method comprise quartz (Qz), K-feldspar (Kfs), plagioclase (Pl), calcite (Cal), dolomite (Dol), amphibolite (Am), pyroxene (Px), Fe-bearing (Fe-b), kaolinite (Kln), smectite (Sme), illite (Ill, including muscovite), chlorite (Chl) and biotite (Bt).

Chronology

The correlation of the physical parameters (wet bulk density, k_{LF} and a^*) measured on cores 02BC and 01PC suggests that ~7 cm of sediments at the top of core 01PC were lost during piston coring (Fig. S1). Therefore, the depth of core 01PC was adjusted and the age–depth model was generated using corrected depths. The chronology of the sediment cores was constrained by nine accelerator mass spectrometry (AMS) radiocarbon (^{14}C) ages (Fig. 2). Eight samples were measured on well-preserved marine shell fragments (mainly *Hiatella arctica*), while one sample was measured on mixed benthic foraminiferal species (Table 1). The mean reservoir age correction from three mollusc shells collected before the nuclear weapons tests (i.e. before 1953; Hua, 2009) near the study area and reported in the updated CALIB Marine Reservoir Database (based on Marine20; Stuiver *et al.* 2017; Heaton *et al.* 2020; http://calib.org/marine/) suggests a ΔR of 157 ±18 years (McNeely *et al.* 2006; Coulthard *et al.* 2010; Dyke *et al.* 2019). Note that the new Marine20 calibration curve induces calibrated ages ~150 years younger than equivalent Holocene ^{14}C ages calibrated with Marine09 or Marine13 (Heaton *et al.* 2020). However, this ΔR value was probably not constant during the last deglaciation and the Holocene, as major oceanic reorganization occurred in northern Baffin Bay at these times (e.g. Jennings *et al.* 2011, 2019; Furze *et al.* 2017; Georgiadis *et al.* 2018; Reilly *et al.* 2019; Hansen *et al.* 2020). Indeed, the complex mixing between Atlantic water from Baffin Bay with a ΔR of 0–140 years (using Marine13, which equates to −150–10 years using Marine20; Georgiadis *et al.* 2018; Caron *et al.* 2019, 2020) and Arctic water with a ΔR of 240–260 years (using Marine13, which equates to 90–110 years using Marine20; Georgiadis *et al.* 2018; Jakobsson *et al.* 2018; Caron *et al.* 2019) makes it difficult to estimate an appropriate ΔR in late Quaternary sedimentary records from northern Baffin

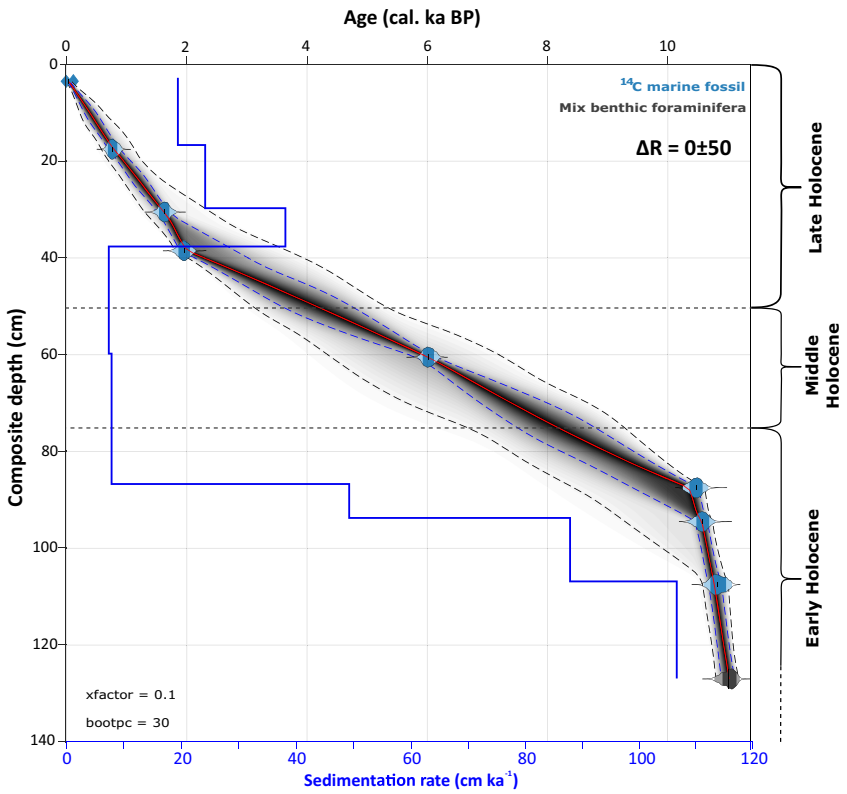

Fig. 2. Bayesian age model and sedimentation rates of cores 02BC and 01PC. The red line is the median probability age, the blue dashed lines represent the 1σ interval for age (68.2%), and the black dashed lines represent 2σ intervals for age (95.4%). Note: the depth is the composite depth of the two cores. Downcore variations in sedimentation rate are shown by the blue line.

Table 1. Accelerator mass spectrometry (AMS) radiocarbon dates and calibrations for cores 01PC and 02BC with different reservoir ages.

Laboratory number	Core	Material dated	Depth (cm)	^{14}C age (a BP)	Error	$\Delta R = 0 \pm 50$		$\Delta R = 150$	
						Median probability	Range 2σ	Median probability	Range 2σ
UCIAMS-233557	02BC	Shell fragment	3	−6	0	35	−13–83	41	6–74
UCIAMS-233558	01PC	Shell fragment	10	1385	15	755	556–1107	621	495–993
UCIAMS-233556	01PC	Shell fragment	23	2210	15	1584	1267–2334	1412	1111–2168
UCIAMS-233559	01PC	Shell fragment	31	2480	15	1978	1782–3583	1783	1637–3409
UCIAMS-233555	01PC	Shell fragment	53	5805	20	5926	4344–7191	5748	4154–7018
UCIAMS-233560	01PC	Shell fragment	80	9725	20	10 255	8363–10 551	10 110	8290–10 334
UCIAMS-233561	01PC	Shell fragment	87	9795	20	10 539	9238–10 723	10 341	9181–10 483
UCIAMS-233562	01PC	Shell fragment	100	9960	20	10 767	10 565–10 991	10 567	10 418–10 708
UCIAMS-239490	01PC	Mixed-benthic foraminefera	120	10 095	20	11 021	10 804–11 177	10 807	10 646–10 993
UCIAMS-239489	01PC	Shell fragment	160	42 000	810	42 042	40 810–43 294	41 927	40 734–43 150

Bay. Taking this into consideration, the conventional ^{14}C ages obtained in this study were calibrated using the Marine20 curve assuming a regional reservoir age correction of $\Delta R = 0 \pm 50$ years, which means that the dates may be older than specified. To account for this, calibrated ages are presented in Table 1 with $\Delta R = 0$ and $\Delta R = 150$ years to illustrate the potential age envelope for the ^{14}C dates. To derive the best age–depth model we used the MATLAB software package 'Undatable' v.1.3.1 (Lougheed & Obrochta 2019) as this program allows: (i) a Bayesian age–depth model to be build based on both the age and depth uncertainties of the ^{14}C dates; and (ii) computation of a conservative age–depth uncertainty, through the provision of bootstrapping and sediment accumulation rate uncertainty (Waelbroeck, 2019). For age–depth modelling, we used the following settings in 'Undatable': nsim = 10^4, bootpc = 30 and xfactor = 0.1 (Lougheed & Obrochta 2019). Although this Bayesian age–depth modelling routine produced a robust age model in core 01PC, we recognize the difficulties associated with establishing accurate age–depth models in marine sediment cores (e.g. Telford *et al.* 2004; Trachsel & Telford 2017; Lacourse & Gajewski 2020).

Statistical approach and sediment unmixing model

The detailed methodologies used for the statistical analysis and sediment unmixing model are presented in Data S2. Briefly, principal component analysis (PCA) was performed on qXRD and pXRF data to identify associations with similar relative variations (e.g. von Eynatten *et al.* 2003; Montero-Serrano *et al.* 2010, 2015). Linear discriminant analysis was also performed with the potential sediment sources to demonstrate the different mineralogical compositions of these sources. We used the nonlinear unmixing Excel macro SedUnMix (version 2014-10-08; Andrews & Eberl 2012; Andrews *et al.* 2015) to gain a quantitative understanding of the downcore changes in bulk sediment provenance.

Results and interpretation

Chronology

According to the proposed age model (Fig. 2), the upper 120 cm of core 01PC spans the last 11 cal. ka BP. This age model reveals three major changes in sedimentation rates during the Holocene: a high sedimentation rate of 106–50 cm ka^{-1} during the Early Holocene (11 to 10.2 cal. ka BP), a pronounced decrease to 8–7 cm ka^{-1} during the Early to Late Holocene (10.2 to 2 cal. ka BP), and an increase after this period to 38–19 cm ka^{-1} during the Late Holocene (2 to 0.2 cal. ka BP). Note that the oldest AMS ^{14}C date (~42 cal. ka BP; Table 1) obtained at the base of core 01PC (160 cm) was excluded from the age model.

Mineralogical and elemental geochemical associations

Boxplots of qXRD data (Fig. 3A) illustrate that cores 02BC and 01PC are dominated by Qz (~19–40 wt.%), Pl (~13–29 wt.%), Kfs (~10–17 wt.%), Cal + Dol (~2–17 wt.%), Bt + Chl (~7–22 wt.%), Ill (~2–15 wt.%) and Sme (~0.8–13 wt.%). These minerals represent more than 90% of the overall mineral concentration of sediments (also see the Supplementary Materials section for additional figures and comments). Furthermore, a boxplot of pXRF data (Fig. 3B) shows that the major element composition of bulk sediments in cores 02BC and 01PC is dominated by Si (~31–81 wt.%), Fe (~13–38 wt.%), Ca (~7–38 wt.%), Al (~4–18 wt.%), K (~6–12 wt.%) and Ti (~2–3wt.%), while the minor and trace elements are dominated by Mn (~96–582 mg kg^{-1}), Zr (~44–279 mg kg^{-1}), Sr (~9–234 mg kg^{-1}) and Rb (~45–80 mg kg^{-1}). Stratigraphic distributions of the qXRD and pXRF data from the two sediment cores studied here are shown in Fig. S2.

PCA of the qXRD data explains 95.3% of the total variance with two principal components (PCs; Fig. 3C): PC1 (70.3%) shows positive scores dominated by Qz, Pl

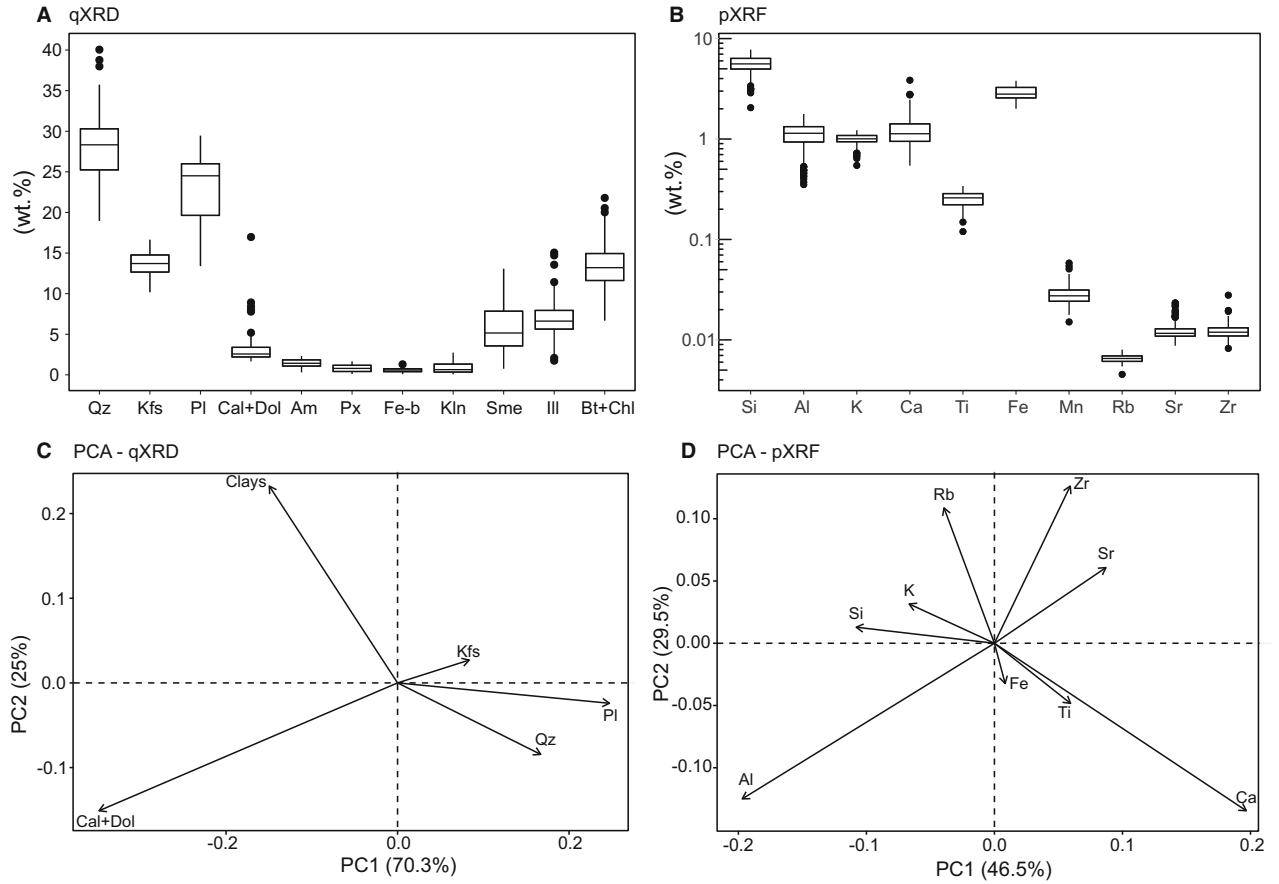

Fig. 3. Results of mineralogical (qXRD) and elemental geochemical (pXRF) composition of the sediment cores studied here. A. Boxplot of the distribution of the main minerals (wt.%) within the cores. B. Boxplot of the distribution of the main elements (wt.%) within the cores. Centered log-ratio biplots obtained from the principal component analysis (PCA) of qXRD (C) and pXRF (D) data of the cores 01PC and 02BC.

and Kfs and negative scores dominated by Cal + Dol and clays; and PC2 (25%) is influenced by Qz, Pl and Cal + Dol (negative scores) and Kfs and clays (positive scores). The PCA of the pXRF data reveals two PCs that explain 76% of the total variance (46.5 and 29.5% for PC1 and PC2, respectively; Fig. 3D) and show a strong influence of Ca, Al and Si. PC1 reveals positive scores mainly controlled by Ca, Sr and Zr variations and negative scores controlled by Al, Si and K. PC2 shows an anti-correlation of Zr and Rb with Al and Ca. Hence, PC1 and PC2 are most likely associated with changes in sediment sources. The mineralogical and elemental geochemical compositions of both cores reveal high concentrations of Si, Al, Fe and Ca, which can be associated with high concentrations of Qz, Pl + Kfs, clays enriched with Fe (Bt + Chl) and Cal + Dol, respectively (Fig. 3C and D). Based on these results, we selected Mn/Al to document changes in oxygenation conditions (Spofforth *et al.* 2008; Jaccard *et al.* 2009; Mouret *et al.* 2009), Zr/Rb as a semiquantitative grain-size indicator (Croudace & Rothwell 2015; Wu *et al.* 2020; Toucanne *et al.* 2021) with a better vertical resolution than discrete grain-size analysis, Ca/K to trace detrital carbonate variations (Croudace & Rothwell 2015), (Bt + Chl)/Pl to trace changes from the Canadian Shield sources (rich in plagioclase) and (Cal + Dol)/clay to trace changes in the detrital carbonate content from rocks in the northern part of the Nares Strait (Fig. 4). pXRF elemental ratios are presented as log ratios to mitigate the amplitude changes in elemental concentrations caused by variable water content, grain-size distribution and irregularities of the split core surface (e.g. Weltje & Tjallingii 2008).

Sediment sources

The linear discriminant analysis and ternary plot Cal + Dol – Pl – Kln + Ill indicate that the four potential sediment sources used in this study (i.e. source 1, Canadian Shield; source 2, Nares Strait - detrital carbonates; source 3, Jones Sound; and source 4, Thule Supergroup) have minerals that allow a reasonable degree of sediment discrimination (Table 2, Fig. 4). The Canadian Shield sources are characterized by a higher Pl proportion, the sediments from Nares Strait are enriched in Cal + Dol, the sediments from the Thule Supergroup are related to higher Kln + Ill and Fe-bearing mineral contents, and the

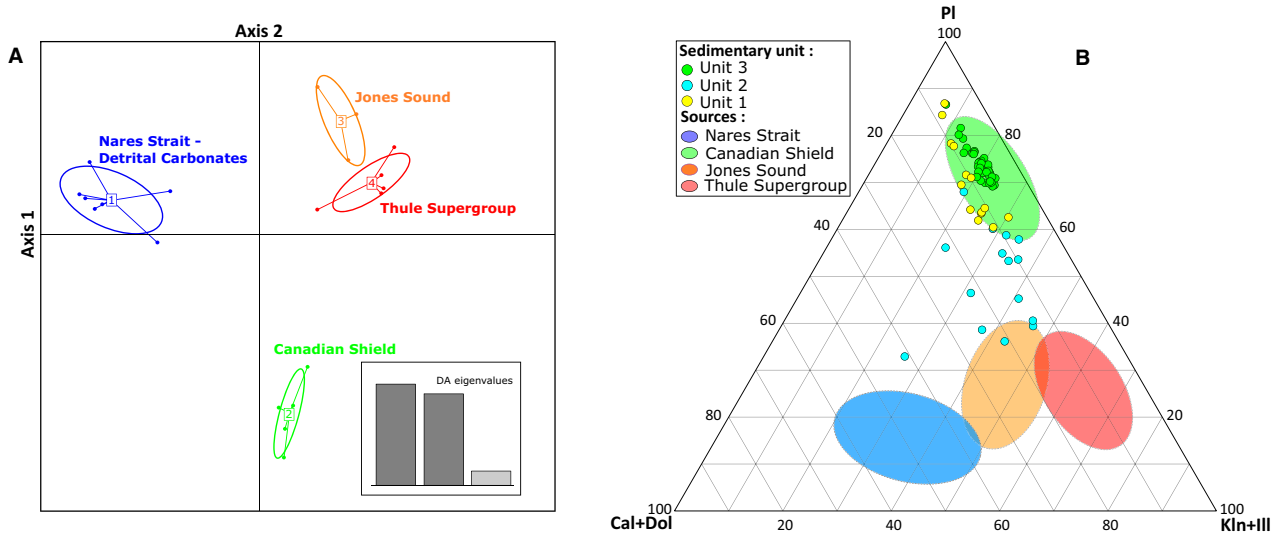

Fig. 4. A. Linear discriminant analysis of the four sediment sources used in this study. The linear discriminant analysis diagram corroborates that potential sediment sources have different mineralogical characteristics that allow a reasonable degree of discrimination. Detrital carbonate data are from Andrews *et al.* (2018), Andrews (2019) and Caron *et al.* (2020), Jones Sound data are from Brossard (2021) and Thule Supergroup data are from Andrews (2019). These sediment sources were then used in the SedUnMixMC modelling. B. Plagioclase (Pl)–kaolinite–illite (Kln + Ill)–calcite+dolomite (Cal + Dol) ternary plot. The coloured ellipses represent mineralogical signatures from the main sources discussed in this study.

sediments from Jones Sound are characterized by intermediate proportions of Cal + Dol and Kln + Ill (Fig. 4B). These results validate the use of these sources in the SedUnMix software. Note that the fraction of source not resolved by the SedUnMix modelling is relatively low (ranging from 1 to 12 wt.%).

Grain size and sortable silt

The grain-size distributions of cores 02BC and 01PC reflect a composition generally dominated by silts and clays, with some samples composed of medium to coarse sand (Fig. 5A–E, G–K). As suggested by McCave & Andrews (2019a, b), we tested the correlation between $\overline{SS}$ and *SS*% to evaluate whether the sortable silt record in both cores was sufficiently current sorted to provide a reliable flow history. A good positive coefficient of correlation ($r = 0.95, n = 66$) was obtained for both cores (Fig. S3B). Likewise, 90 and 88% of the data have a five-point running downcore correlation (r_{run}) between $\overline{SS}$ and *SS*% of >0.5 and a slope relationship of >0.07 (Fig. S3E, F). These results suggest that much of the sortable silt records in cores 02BC and 01PC are well sorted. Bivariate plots of the *SS*%, $\overline{SS}$ and fine sand fraction (63–250 μm) in both cores illustrate a bias towards coarser silt grain sizes as the fine sand content increases (Fig. S3C, D). Notably, samples with higher $\overline{SS}$ and *SS*% also have higher fine sand contents.

Sedimentary units

Sedimentary units (lithofacies) were determined based on visual descriptions of the core photography, X-CT scan images, physical properties and grain-size parameters (Fig. 5). Considering these observations, core 01PC shows three distinct sedimentary units or lithofacies (Fig. 5). Core 02BC comprises the last sedimentary unit (Unit 3) of core 01PC (Fig. S1). These sedimentary units labelled 1–3 from base to top are described and interpreted below according to core depth.

Core 01PC. – Unit 1 (198–124 cm; prior to ~11 cal. ka BP) is silty mud with centimetre- to millimetre-scale sandy laminae, with high variations in grain size, absence of cross-lamination, low foraminifera content (Fig. S4) and lack of bioturbation (based on the X-CT scan images; Figs 5, 6, 7). The high percentage (up to 48 wt.%) of fine sand fractions (62–125 and 125–400 μm) compared with that of the coarse fraction (up to 17 wt.%) reflects a strong sediment transport dynamic (Fig. 5M). X-CT scan images show that the thickness and sand content of these sandy laminae decrease progressively upward from the unit (Figs 5, 6), suggesting a loss of intensity of sedimentary transport. Thin sections reveal that basal laminae are composed of heterogeneous angular fine to medium sand with isolated gravel-sized clasts, which can be identified as IRD (Fig. 7A, B). All laminae at the base of the unit are constituted by two layers: first, coarsening upward from very fine silt-clay to fine-medium sand; and a second, fining upward from fine-medium sand to very fine silt-clay (Fig. 7B). These sequences exhibit a typical hyperpycnite deposit, i.e. a basal coarsening-up unit deposited during the waxing period of subglacial discharges, followed by a top fining-up unit deposited during the waning period of subglacial discharge (Mulder *et al.* 2003). Similar sandy laminae

Table 2. Average mineralogical composition for the main sources used in the SedUnMix modelling and discussed in this study. Detrital carbonates (Nares Strait) data are from Caron *et al.* (2020), Andrews *et al.* 2018 and Andrews (2019), Jones Sound data are from Brossard (2021) and Thule Supergroup data from Andrews (2019).

Minerals	Nares Strait		Canadian Shield		Jones Sound		Thule Supergroup	
	(*n* = 7) Average	SD	(*n* = 7) Average	SD	(*n* = 3) Average	SD	(*n* = 6) Average	SD
Quartz	18.86	6.13	27.66	2.91	12.62	0.51	14.62	6.65
K-feldspar	9.11	1.95	13.14	2.63	8.33	1.36	10.73	1.01
Plagioclase	8.51	2.23	25.58	2.90	10.54	3.06	14.47	2.36
Calcite	16.05	3.51	0.43	0.78	0.10	0.00	0.10	0.00
Dolomite	14.65	2.51	1.80	0.19	9.75	2.90	6.20	1.54
Amphibole	0.65	0.33	2.05	1.08	2.57	0.45	0.88	0.60
Pyroxene	0.53	0.50	0.53	0.41	0.34	0.13	0.58	0.50
Fe-bearing	0.41	0.16	0.45	0.19	0.33	0.18	1.53	0.42
Kaolinite	2.68	2.41	0.50	0.42	1.75	0.91	0.55	0.41
Smectites	7.59	1.48	4.69	2.18	12.68	3.30	5.30	2.71
Illites	10.17	2.91	5.28	1.62	9.43	1.95	16.33	4.88
Biotite and chlorite	8.97	1.17	11.35	5.34	10.47	0.31	11.00	1.45

have been reported in other glacial marine studies that address ice-proximal sedimentology (e.g. Dowdeswell & Cromack 1991; Ó Cofaigh & Dowdeswell, 2001; Jennings *et al.* 2011, 2019; Ó Cofaigh *et al.* 2013; Pieńkowski *et al.* 2013; Reilly *et al.* 2019). Following the decrease in thickness and sand content of these laminae, an increase in cohesive particles (<10 μm; Fig. 5H, I) and a decrease in $\overline{SS}$ (Fig. 6A) confirm a decrease in sediment transport intensity. The vertical distributions of ln(Zr/Rb) and ln (Mn/Al) show high variations (Fig. 6F), in accordance with the laminae occurrence and observed changes in grain size. ln(Ca/K) and *a** are low and have constant values throughout the unit. Unit 1 is largely dominated by sediments from the Canadian Shield (Fig. 6D), but this input of sediment progressively decreases, and a progressive increase in Jones Sound sediments occurs (Fig. 6C). The transition with Unit 2 occurs gradually and is marked by the disappearance of laminations. Overall, the sedimentological characteristics of Unit 1 suggest that the core location was close to a grounded ice zone influenced by subglacial meltwater discharges (e.g. Gilbert 1982; Reilly *et al.* 2019; Fig. 9A).

Unit 2 (124–57 cm; ~11 to 6.6 cal. ka BP) corresponds to silty mud with some fine sand intercalations with low percentages (~7 wt.%) of 63–125 and 125–400 μm sand fractions and isolated increases in the coarse sand fraction (>400 μm; identified as IRD; Fig. 6M). A granitic rock fragment was found at 112–104 cm. Four gravel-sized layers (IRD) are present in this unit at ~124, ~98, ~80 and 57–67 cm (Fig. 5G). A slight increase in non-cohesive silt and a decrease in cohesive silt occurred in this unit (Fig. 5H-J). The $\overline{SS}$ profile shows lower values near 100 cm (~20 μm), which increase progressively until the end of the unit (up to 25 μm; Fig. 6A). The ln(Zr/Rb) and ln(Mn/Al) seem to follow $\overline{SS}$ variations (Fig. 6A, F). The ln(Ca/K) and (Cal + Dol)/clay ratios have low values at the base of the unit to 80 cm and increase progressively up to 67 cm and markedly up to the top of this unit (Fig. 6B, G). This increase could be associated with the increase in detrital carbonates from north of Nares Strait (Fig. 6C). The *a** shows a pronounced increase at 115 cm before a dropstone and until the top of the unit (Fig. 5L). The maximum value of *a** corresponds to the strong increase in sediments derived from the Thule Supergroup, which is enriched in red sediments (Fig. 6D). The top of Unit 2 is marked by a complete decrease in sediment input from Nares Strait, the Thule Supergroup and Jones Sound to make way for a total provenance (near 100%) input from the Canadian Shield. A significant change in grain size and mineralogical and elemental ratios marks the transition between Unit 2 and Unit 3 (Figs 5, 6). Altogether, Unit 2 is interpreted to reflect an increasingly ice-distal environment following regional deglaciation, dominated by hemipelagic sedimentation and suspension settling from turbid meltwater plume overflows (Fig. 9B; Gilbert 1982).

Finally, Unit 3 (57–0 cm; 6.6 cal. ka BP to present day) is silty sandy mud with strong variations in sand fractions (Fig. 5H–K, M). The $\overline{SS}$ (Fig. 6A) and sand profiles (Fig. 5K, M) show higher values between 57 and 30 cm, which decrease progressively to the top of the unit. The cohesive fraction (low at the base of the unit) is anti-correlated to the $\overline{SS}$ profile (Fig. 5H-I). A lower content of gravel-sized clasts is observed between 57 and 30 cm in comparison with the upper part of the unit (Fig. 6A). The SedUnMix results indicate a dominant source from the Canadian Shield (Fig. 6D). Two granitic rock fragments are also visible in the core photographs at ~55 and ~8 cm (Fig. 5), making it difficult to count the gravel-sized clasts on the X-CT scan images in these intervals. High ln(Mn/Al) values are recorded between 57 and 40 cm (Fig. 6I). Note that Fe/Al and Mn/Al display a positive linear correlation (r = 0.91; Fig. S3A) in this unit, indicating a geochemical relationship that is most likely associated with Fe–Mn oxyhydroxide phases (e.g. Macdonald & Gobeil 2012; Gamboa *et al.* 2017). The ln(Zr/Rb) and ln(Mn/Al)

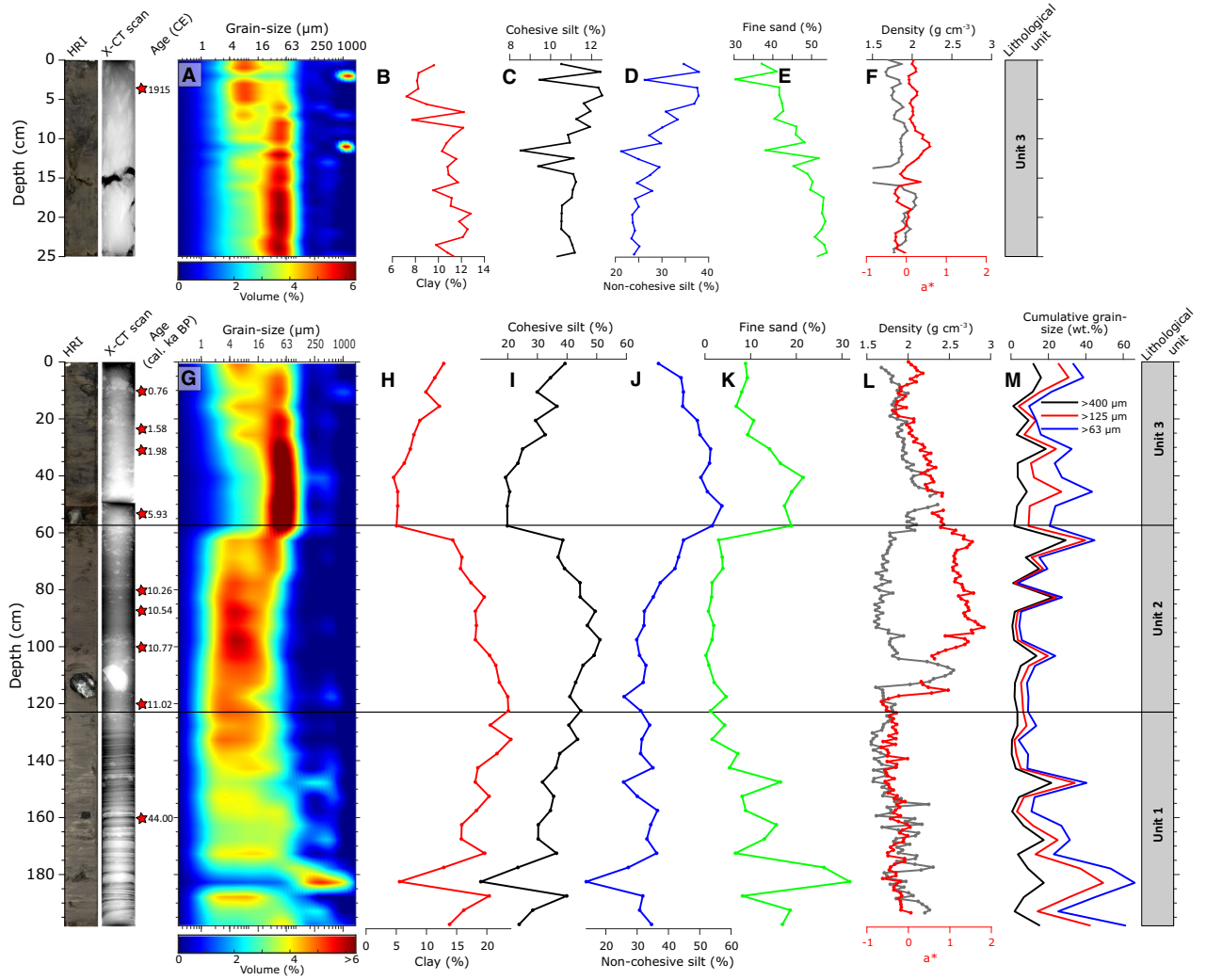

Fig. 5. High-resolution core photography, X-CT scan image, grain-size parameters and physical properties of cores 02BC (A–F) and 01PC (G–M). A, G. Interpreted modal distributions of grain size. B, H. Percentages of clay fraction (%). C, I. Percentages of cohesive silt fraction (%). D, J. Percentages of non-cohesive silt fraction (%). E–K. Percentages of fine (63–250 μm) sand fraction (%). F, L. Density (grey) and a^* red colour indicator (red). M. Cumulative sand fractions of core 01PC (wt.%). Note that 1) the y scales of core photography and X-CT scan images are stretched and 2) the radiocarbone age in core 02BC is expresed in calibrated years Common Era (CE).

ratios show a continuous decrease throughout the unit associated with a progressive increase in (Bt + Chl)/Pl beginning at ~40 cm (Fig. 6B, F). Overall, the sedimentological characteristics of Unit 3 suggest that two sedimentary processes operate in this unit. The interval between 57 and 30 cm was probably deposited in a distal glacial marine setting influenced by meltwater outwash and sea-ice rafting (Fig. 9C; Powell 1981). Conversely, the last 30 cm of the unit reflects sediment deposition influenced by ice fronts advancing towards the coast, which promote the release of icebergs and large inputs of rock-flour-laden meltwater into the inlet (Fig. 9D).

Core 02BC. – Core 02BC corresponds to the top of Unit 3 of core 01PC (silty sandy mud) (Fig. S1). No significant changes in the grain size (Fig. 5A–F) or mineralogical and elemental geochemistry profiles (Fig. 8) are visible in the first half of the core (25–15 cm). The upper half of the core is characterized by an increase in cohesive silt and clay contents, higher (Bt + Chl)/Pl values, lower ln(Zr/Rb) (Figs. 8B and 8E) and a steady decline in $\overline{SS}$ values (Fig. 8A). X-CT scan images and the number of >2 mm clasts show that gravel-sized clasts are more frequent between 10 and 14 cm. Higher ln(Mn/Al) values are also recorded in this interval, probably linked to an increase in iceberg calving.

Discussion

Here the sedimentary environments and depositional processes interpreted from the sedimentary units are used to document the impact of ice–ocean interactions on sediment dynamics in northwestern Baffin Bay

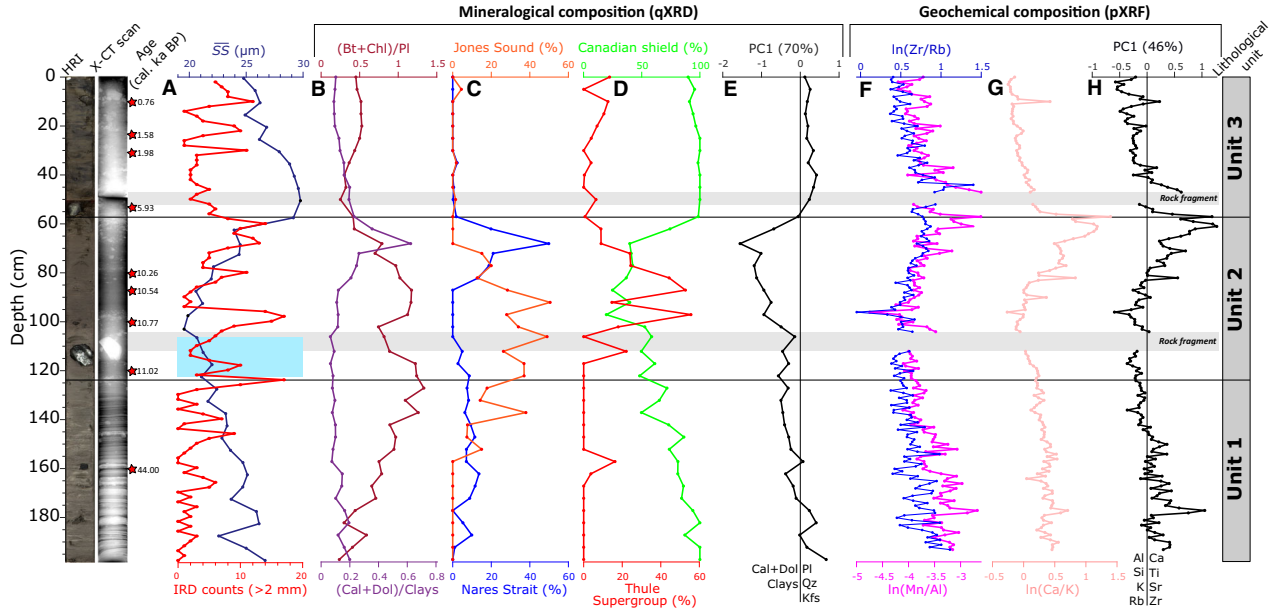

Fig. 6. Proxies used for core 01PC. From left to right: high-resolution core photography; X-CT image. A. Mean size of sortable silt fraction (μm) and >2 mm (count no.) profiles. The blue area indicates sections of the sortable silt record that do not pass the reliability test of a downcore correlation coefficient >0.5 between *SS* and *SS*% (McCave & Andrews 2019a). B. (Bt (biotite) + Chl (chlorite))/Pl and (Cal + Dol)/clay profiles. C, D. SedUnMix results with the proportions of sediment from Jones Sound (orange), the Nares Strait (blue), the Canadian Shield (green) and the Thule Supergroup (red). E. principal component 1 (PC1; qXRD) scores (70%). F. ln(Zr/Rb) and ln(Mn/Al) ratio profiles. G. ln(Ca/K) ratio profile. H. PC1 scores (46%); sedimentary units.

during the last deglaciation and reconstruct the activity of Cape Norton Shaw glaciers during the Holocene.

Glacial sediment dynamics (prior to ~11 cal. ka BP). – In agreement with palaeoreconstructions performed around the study area (e.g. England *et al.* 2006; Jennings *et al.* 2019; Dalton *et al.* 2020), we hypothesize that Unit 1 was deposited between 13 and 11 cal. ka BP during the deglaciation phase of the IIS (Fig. 9A,E). The sedimentary dynamics at this time are thought to have been dominated by the retreat of the glacier grounding line through the inlet (Fig. 9A). We infer that the high boreal summer insolation, strong seasonal contrasts and warmer air temperatures (Berger & Loutre 1991; Thomas *et al.* 2010; Lecavalier *et al.* 2017; Fig. 10A) that prevailed in the study area during the deglacial/Early Holocene (12 to 8.2 cal. ka BP; Walker *et al.* 2012) probably promoted large hyperpycnal flows of sediment-laden subglacial meltwater in Cape Norton Shaw Inlet. Furthermore, the dated shell fragment at 160 cm in core 01PC indicates an age of ~43.9 cal. ka BP, suggesting that Unit 1 is composed of reworked subglacial sediments deposited before the last glaciation. Shells older than 30 ka BP have been reported in glaciomarine deposits close to the Manson Icefield area (Makinson Inlet and Piliravijuk Bay; Hodgson 1985; Blake 1993). These shells could be entrained by the IIS and carried to Cape Norton Shaw Inlet during the LGM and subsequently remobilized by the retreat of the grounding zone to the innermost Cape Norton Shaw Inlet during the last deglaciation (Fig. 9A). The strong vertical variability in the wet bulk density and ln(Zr/Rb) and ln(Mn/Al) ratios (Fig. 7) and the high quartz and feldspar contents (Fig. S2) observed in Unit 1 support the idea that coarse sandy laminae are composed of reworked subglacial sediments derived from glacial erosion of the Canadian Shield bedrock.

Early to Middle Holocene sediment dynamics (~11 to 6.6 cal. ka BP). – Higher boreal summer insolation in the Early Holocene led to a period of warmer than present conditions that are expressed well in most palaeoclimate records (Thomas *et al.* 2010; Fig. 10A). The seasonality was strong in the Early Holocene because of important differences in solar insolation (Berger & Loutre 1991; Fig. 10A), with warm and short summers owing to the shrinking Laurentide Ice Sheet (Kaplan & Wolfe 2006). In this context, summer temperatures were high in the Early Holocene, whereas mean annual temperatures revealed a period of warming during the Middle Holocene. The deglaciation of eastern Smith Sound is captured in core 01PC by an increase in fine-grained red sediments from the Thule Supergroup at ~11 to 10.65 cal. ka BP (Unit 2; Fig. 10D, I). This mineralogical evidence also marks the beginning of the cyclonic current formation of the WGC in Smith Sound (Jennings *et al.* 2019; Fig. 9E). Thus, the maximum proportion of sediments from the Thule Supergroup recorded at 10.65 cal. ka BP in core 01PC could correspond to the transition from pervasive sea-ice cover

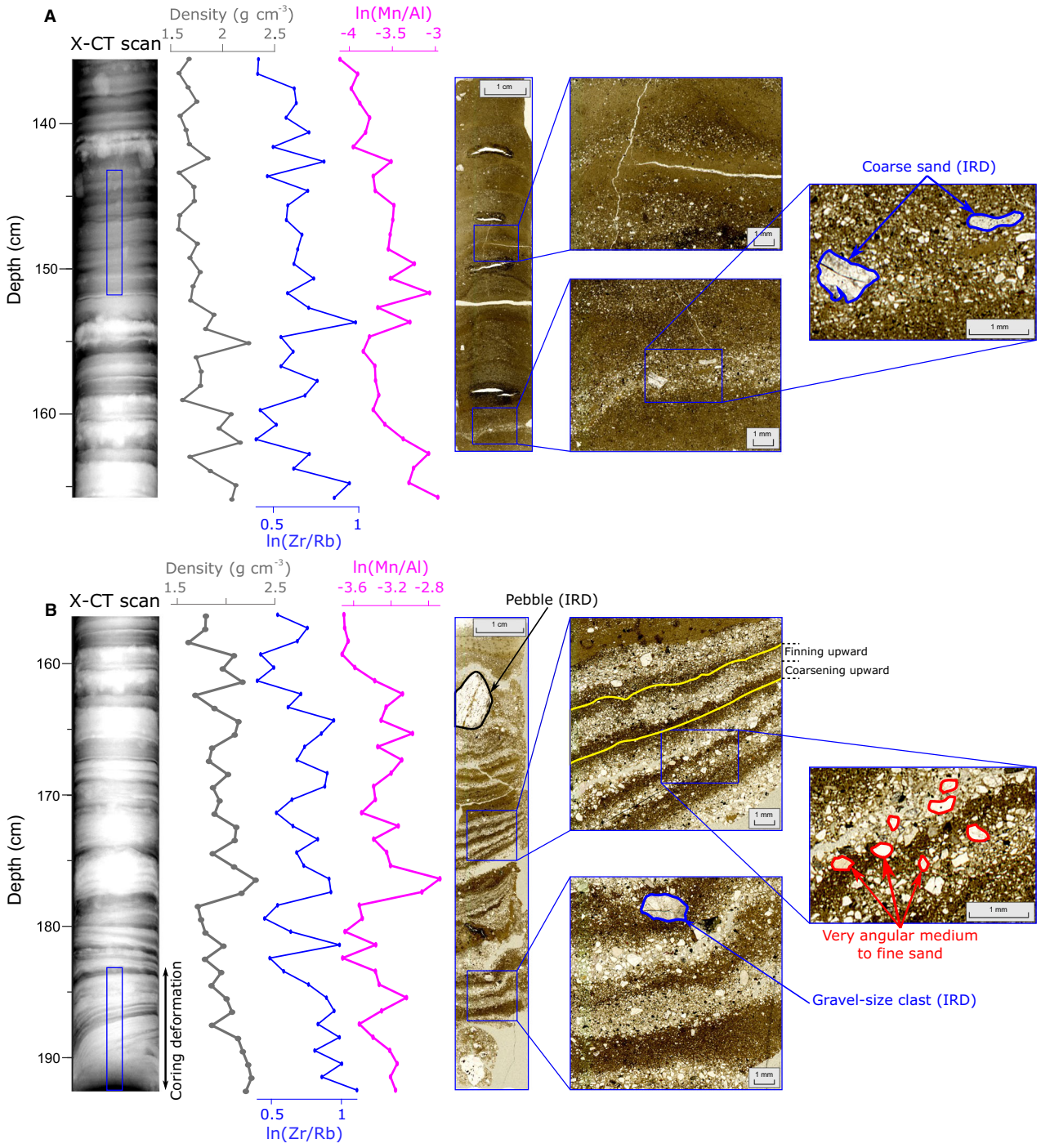

Fig. 7. High-resolution core photography, X-CT scan image, wet bulk density, ln(Zr/Rb), ln(Mn/Al) profiles and thin sections of the top (A) and base (B) of Unit 1 in core 01PC. A. Millimetre-scale sandy laminae with very angular ice-rafted debris (IRD) alternating with silty laminae. B. Millimetre-scale hyperpycnite with very angular clasts and with isolated pebble and gravel-sized clast (identified as IRD).

to more open glacial marine conditions associated with seasonal sea-ice melting in Smith Sound and the opening of the NOW (Fig. 9B,F), estimated at 10.4 cal. ka BP by Jennings *et al.* (2019). Core 042PC from southeastern Coburg Island (Fig. 1A) was studied by St-Onge & St-Onge (2014) and does not record this increase in red colour. This difference could be explained by a situation where the cyclonic current of Smith Sound has deposited sediments from the Thule Supergroup at Cape Norton Shaw Inlet, whereas those sediments are expelled from south of Coburg Island by the freshwater export from Jones Sound glaciers (Fig. 9F). This interpretation agrees with the synthesis of ice-sheet reconstructions of Dalton *et al.* (2020).

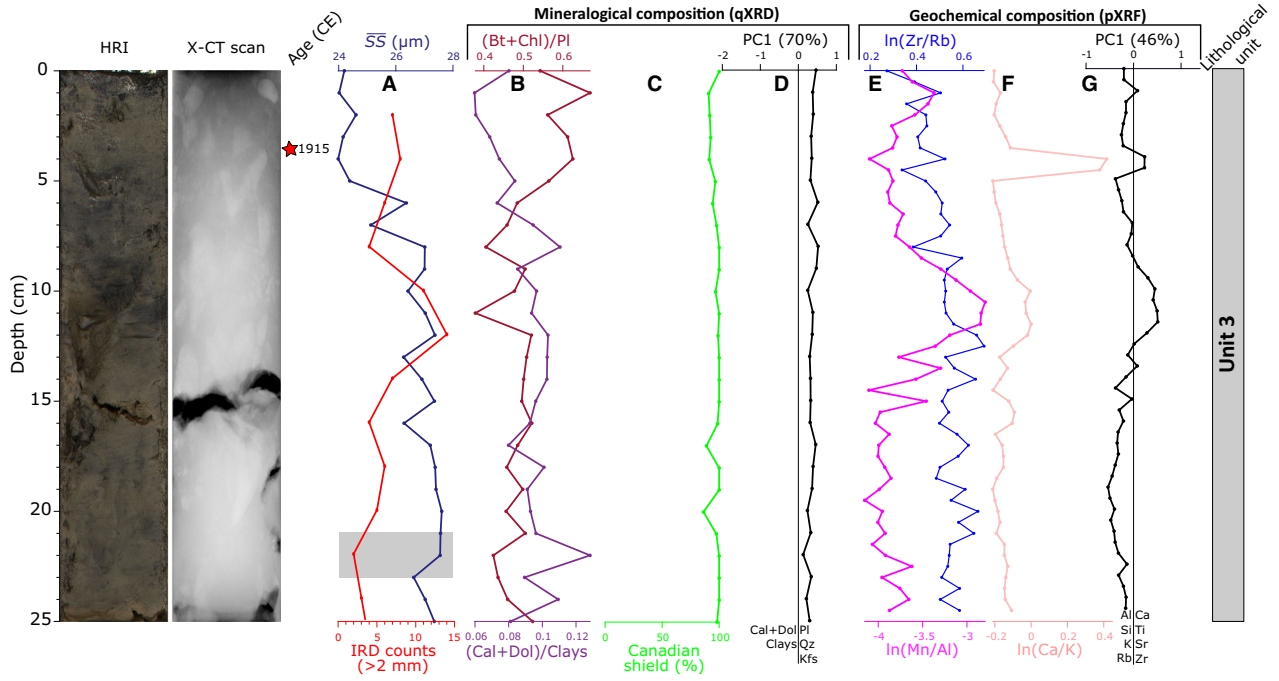

Fig. 8. Proxies used for core 02BC. High-resolution photography; X-CT image; The radiocarbone age is expresed in calibrated years Common Era (CE). A. Mean size of sortable silt fraction (µm) and >2 mm (count no.) profiles. The blue area indicates sections of the sortable silt record that do not pass the reliability test of a downcore correlation coefficient >0.5 between *SS* and *SS*% (McCave & Andrews 2019a). B. (Bt + Chl)/Pl and (Cal + Dol)/clay profiles. C. SedUnMix results with the proportions of sediment from the Canadian Shield (green). D. PC1 (qXRD) scores (70%). E. ln(Zr/Rb) and ln(Mn/Al) ratio profiles. F. ln(Ca/K) ratio profile. G. PC1 scores (46%).

The IRD-rich interval observed between 10.69 and 10.75 cal. ka BP (Unit 2; 95–100 cm; Fig. 6) in core 01PC could be associated with the retreat of the glacier grounding line towards the shoreline and/or the innermost part of the inlet. We estimate that this event could suggest the beginning of glacial marine conditions in the Cape Norton Shaw area (Fig. 9C). Furthermore, the increased influence of sediment inputs from Jones Sound, which begins at the end of Unit 1 and lasts until 10.5 cal. ka BP (Fig. 6C), is probably associated with the progressive break-up of the Jones Sound ice shelf. The decrease in these sediment inputs after ~10.7 cal. ka BP may indicate the complete deglaciation of the eastern part of Jones Sound at this time (Fig. 9F). This interpretation agrees with reconstructed patterns of IIS retreat in the Jones Sound area during deglaciation (Dyke & Evans 2003; Dalton *et al.* 2020).

Previous marine geology studies have proposed an interval from 9.0 to 8.3 cal. ka BP for the complete opening of Nares Strait (Jennings *et al.* 2011, 2019; Georgiadis *et al.* 2018; Caron *et al.* 2019, 2020). The ln (Ca/K) and (Cal + Dol)/clay ratios and IRD content show an increase after the deglaciation of Kennedy Channel between 9.3 and 9 cal. ka BP (Jennings *et al.* 2019) and show a similar trend to the (Cal + Dol)/clay ratios of core AMD14-Kane2b located in Kane Basin (Caron *et al.* 2020; Fig. 10E-G). These results suggest a period of high carbonate-rich IRD export from Nares Strait to northern Baffin Bay between 9 and 6.6 cal. ka BP, in line with the progressive development of the Arctic–Atlantic throughflow during this time (Jennings *et al.* 2019).

Middle to Late Holocene sediment dynamics (6.6 to 2 cal. ka BP). – This period marks the beginning of the marine optimum, with more open marine glacial conditions and a relative sea level close to that of the present day (e.g. Blake 1993). This marine optimum is characterized by higher sea surface temperature and increasing influence of the WGC in northern Baffin Bay (Ledu *et al.* 2010; Caron *et al.* 2019; McCave & Andrews, 2019b; Hansen *et al.* 2020; Weiser *et al.* 2021; Fig. 10C). The low sedimentation rate (~7 cm ka^{-1}; Fig. 2), together with high levels of coarse silt and fine sand, observed in core 01PC during the Middle Holocene, provides evidence for an accelerated landward retreat of the Cape Norton Shaw glaciers. Indeed, when the glacier terminus retreats from tidewater and becomes terrestrial, glacial outwash plains and deltas form (Powell 1981). In this environment, glacial meltwater streams can introduce both sand- and gravel-sized sediments over fan deltas and a mixture of fine-grained sand along with glacial flour silt in more distal marine locations (Powell 1981; Cofaigh *et al.* 2013; Dowdeswell *et al.* 2015; Hogan *et al.* 2020). Moreover, since glacial meltwaters play a predominant role in the input of Fe–Mn oxides in glacial environments

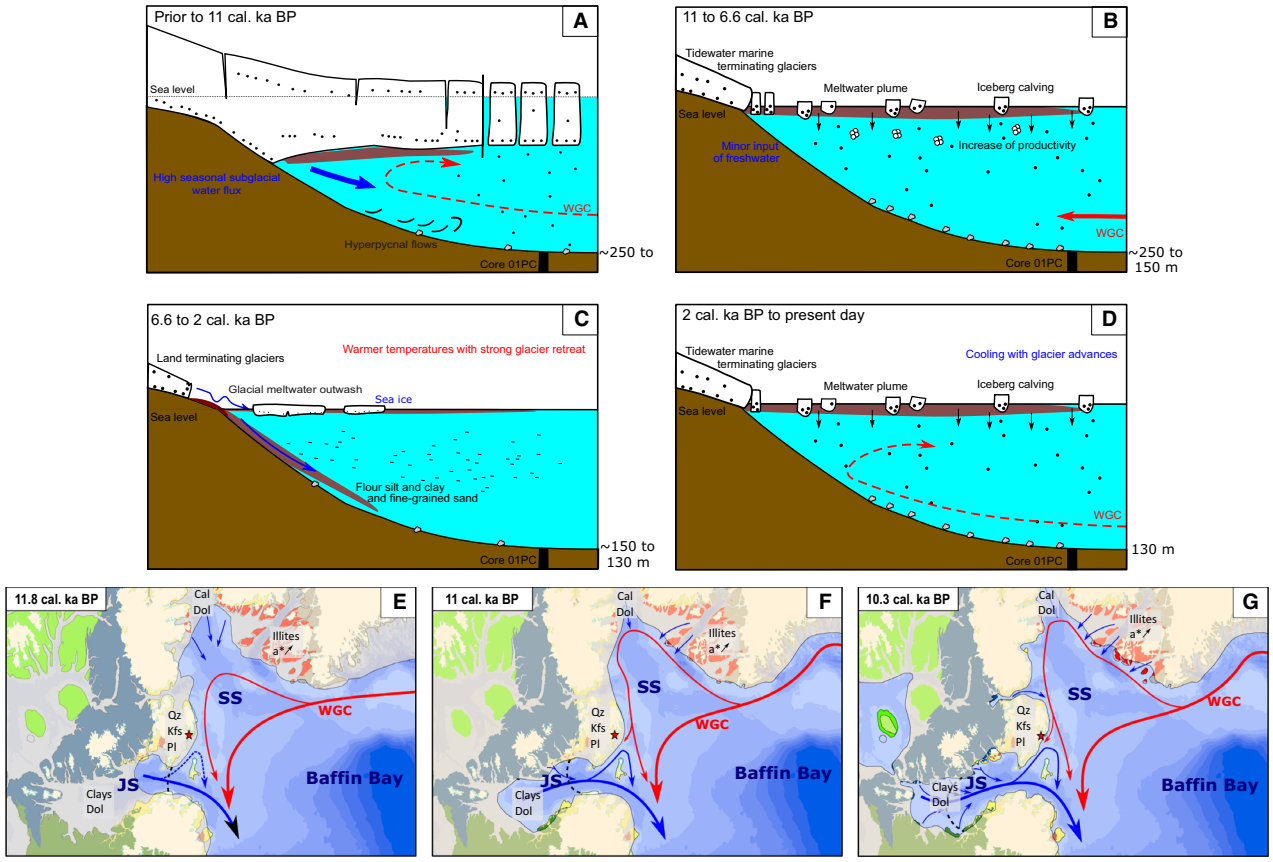

Fig. 9. A–D. Schematic models of sedimentary processes and environmental conditions in Cape Norton Shaw Inlet. A. Prior to 11 cal. ka BP. B. 11 to 6.6 cal. ka BP. C. 6.6 to 2 cal. ka BP. D. 2 cal. ka BP to present day. Grey stones at the bottom represent IRD or dropstone deposits. E–G. Hypothesized oceanographic reconstructions of northern Baffin Bay at 11.8 cal. ka BP (E), 11 cal. ka BP (F) and 10.3 cal. ka BP (G). Blue lines represent surface meltwater; red lines represent the West Greenland Current (WGC). SS = Smith Sound; JS = Jones Sound. Note that all glaciological maps are from Dalton *et al.* (2020).

(e.g. Poulton & Raiswell 2005), we hypothesize that the high ln(Mn/Al) values recorded between 7 and 2 cal. ka BP in core 01PC (Fig. 6F) are related to a higher input to the inlet of preformed Fe–Mn oxyhydroxides associated with detrital fractions.

Furthermore, the $\overline{SS}$ records obtained in cores from both Cape Norton Shaw Inlet and Smith Sound (2001LSSL-014PC; McCave & Andrews, 2019b) indicate strong bottom current velocity during the Middle Holocene (notably 7 to 5 cal. ka BP), which decreased progressively during the Middle to Late Holocene, in line with the further decrease in boreal summer insolation (Fig. 10A, G). However, the fact that fine sand, non-cohesive silt (Fig. 5J, K) and $\overline{SS}$ profiles (Fig. 6A) in core 01PC show a parallel temporal evolution during this interval suggests that glacial meltwater outwash (composed mainly of sand- and silt-sized particles) and sea-ice rafting have a significant influence on the $\overline{SS}$ record in core 01PC, enabling inferences to be made about bottom current speeds. Likewise, previous studies investigating the Holocene evolution of sea-surface conditions in northern Baffin Bay and Kane Basin suggest a longer duration of the open-water season in northern Baffin Bay during the Middle Holocene (Caron *et al.* 2019; Jennings *et al.* 2019). Such conditions could have fostered the recurrent incorporation of proglacial outwash sediments into both sea ice via suspension freezing and anchor ice, and their subsequent entrainment by surface currents through the inlet (e.g. Reimnitz *et al.* 1987; Darby 2003). Under this context, we hypothesize that the coarsening of silt-sized material in core 01PC during the Middle Holocene could be attributed to an enhanced input of sea-ice-rafted sediments to the inlet rather than an increase in the bottom current speed. This interpretation is consistent with previous sedimentological studies performed in regions heavily influenced by sea-ice dynamics, including coastal polynyas (e.g. Reimnitz *et al.* 1993; Nürnberg *et al.* 1994; O'Regan *et al.* 2014; Deschamps *et al.* 2018; Letaïef *et al.* 2021).

Late Holocene to modern sediment dynamics (2 cal. ka BP to present day). – The Late Holocene in the Arctic is characterized by a cooling trend driven by a long-term decrease in boreal summer insolation (Fig. 10A), which

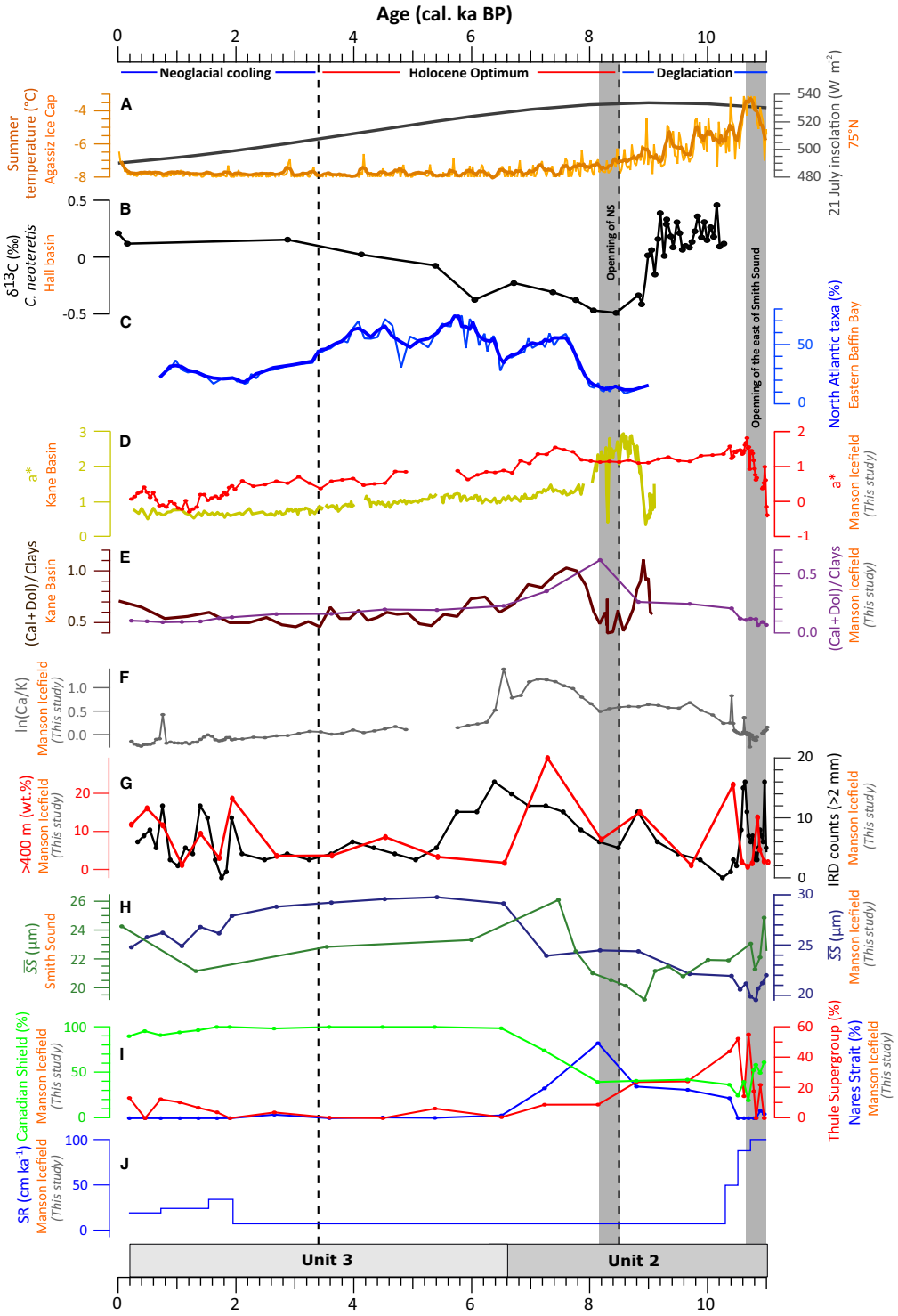

Fig. 10. Comparison of proxies used in this study for core 01PC (in age) with palaeoenvironmental proxies. A. Reconstructed summer temperature (°C) of the Agassiz Ice Cap (Lecavalier *et al.* 2017) and 21 July insolation at 75°N (Laskar *et al.* 2004). B. δ^{13}C (‰) of *C. neoteresis* from core HLY03-05GC (Hall Basin; Jennings *et al.* 2011). C. North Atlantic dinokyste taxa (%) from core AMD14-204 (Caron *et al.* 2019). D. Colour parameter *a** from core AMD14-Kane2b (light green, Caron *et al.* 2019) and from core 01PC (red, this study). E. (Cal + Dol)/clay ratios from core AMD14-Kane2b (dark green, Caron *et al.* 2019) and from core 01PC (dark brown, this study). F. ln(Ca/K) ratio from core 01PC (this study). G. IRD count (>2 mm) of core 01PC (black, this study) and >400 µm in wt.% (red, this study). H. Mean size of sortable silt fraction from cores 01PC (purple, this study) and 2001LSSL-014PC (green, McCave & Andrews, 2019b). I. Mineralogical influences (%) of the Canadian Shield (green, this study), Thule Supergroup (red, this study) and Nares Strait (blue, this study). J. Sedimentation rate (cm ka^{-1}) of core 01PC (this study). Grey areas mark the range of the opening of Nares Strait and Smith and Jones Sounds.

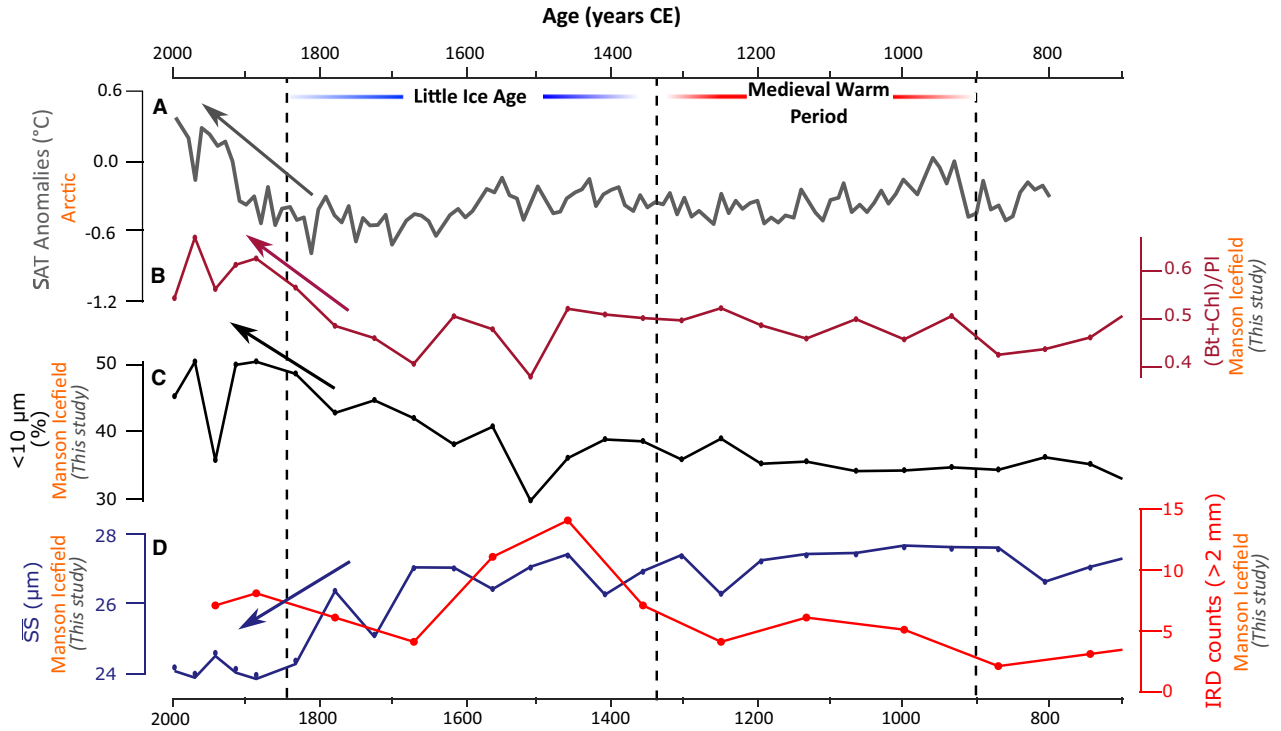

Fig. 11. Comparison of proxies used in this study for core 02BC (in age) to a palaeoenvironmental proxy. A. Surface air temperature (SAT) anomalies in the Arctic (Kaufman *et al.* 2009). B. (Bt + Chl)/Pl profile. C. Cohesive grain fraction (volume %) profile. D. Mean size of the sortable silt fraction (µm, purple curve) and the IRD count (>2 mm, red curve) as an IRD indicator. Ages are expresed in calibrated years Common Era (CE).

corresponds to the Neoglacial period associated with glacier growth (e.g. Solomina *et al.* 2015) and cooler surface waters (e.g. Ledu *et al.* 2010; Caron *et al.* 2019). In Cape Norton Shaw Inlet, the high sediment accumulation rates (~16–26 cm ka^{-1}; Fig. 2) recorded after ~2 cal. ka BP, together with the upward increase in fine silts and clay content and the (Bt + Chl)/Pl ratio in core 01PC (Figs 5H, 6B), provide evidence for an increase in glacial erosional processes within the inlet during this time. Indeed, glacial erosion typically generates a large amount of glaciogenic sediment (rock flour), which can then be transported by meltwater streams and deposited in distal glacial marine settings (e.g. Ó Cofaigh *et al.* 2013; Dowdeswell *et al.* 2015; Hogan *et al.* 2020). Thus, we speculate that the cooler conditions associated with Neoglaciation promoted a greater advance of Cape Norton Shaw glaciers towards the coast, which contributed to the enhanced input of glacially eroded sediments to the inlet (Fig. 9D). In addition, although the $\overline{SS}$ record in core 01PC shows a slight slowdown of the bottom current velocity in the inlet after 2 cal. ka BP (Fig. 10G), which is in line with the Neoglacial slowdown documented off the SW Greenland margin (Weiser *et al.* 2021) and in the North Atlantic (McCave & Andrews, 2019b), our results suggest that increased input and advection of fine-grained sediments in the Cape Norton Shaw Inlet during this period most likely had a strong overprint on the $\overline{SS}$ record in core 01PC.

As no ^{210}Pb and ^{137}Cs analyses were performed to improve the chronology for core 02BC, the variations in the detrital proxies in this core since 800 Common Era or CE will only be used to robustly explore the potential impacts of the Medieval Warm Period (~900–1350 CE; Bradley 2003; Spielhagen *et al.* 2011), Little Ice Age (LIA; ~1350–1850 CE; Jones & Mann 2004) and modern warming (late 1800s CE; Jones & Mann 2004; Kaufman *et al.* 2009) on the sedimentary dynamics of the Cape Norton Shaw glaciers. During the Medieval Warm Period (Fig. 11), which is a climatic period characterized by Arctic summer temperatures warmer than those in the pre-industrial period (Kaufman *et al.* 2009), our grain-size parameters (Fig. 11C–D) suggest that sedimentary regimes in the Cape Norton Shaw Inlet were mainly driven by snowmelt runoff and meltwater plumes during the spring/summer season with a lower iceberg calving rate. Following this warm period, colder conditions associated with the LIA are regionally established (e.g. Cormier *et al.* 2016). In the Arctic, the LIA is characterized by a period of glacier growth (Solomina *et al.* 2015), summer sea surface temperatures an average of 0.6 °C cooler than at present, and an increase in the duration of sea-ice cover in northern Baffin Bay (Cormier *et al.* 2016).

The high coarse ice-rafted clast contributions recorded during this period suggest that such cold climatic conditions promoted glacier growth and increased iceberg calving activity in the Cape Norton Shaw Inlet at this time. The sharp rise in the ln(Mn/Al) ratio and gravel-sized clasts in the middle of this period (Fig. 8E) could be associated with enhanced settling of Fe–Mn oxyhydroxide particles onto the sea floor promoted by high iceberg calving activity in the inlet.

Finally, the progressive increase in the fine silt and clay contents and (Bt + Chl)/Pl ratio (Fig. 11B, C) since ~1800s CE suggest an increase in snowmelt runoff and glacial meltwater plumes from the Cape Norton Shaw glaciers, probably related to the influence of anthropogenic warming (Kaufman *et al*. 2009) and a retreat of marine-terminating glaciers in the Cape Norton Shaw Inlet (Sharp *et al*. 2014; Cook *et al*. 2019). The similar trend observed between the (Bt + Chl)/Pl ratio and fine-grained fraction (Fig. 11B, C) in core 02BC and the Arctic surface air temperature anomalies (Kaufman *et al*. 2009; Fig. 11A) supports the idea that increased atmospheric temperature is one of the main factors driving the acceleration in marine-terminating glacier frontal retreat in the CAA during the industrial period (Noël *et al*. 2018; Cook *et al*. 2019).

Conclusions

The physical, mineralogical and geochemical properties of two sediment cores (02BC and 01PC) recovered from Cape Norton Shaw Inlet highlight the evolution of the composition, provenance and transportation processes of the detrital sediments in the southeastern part of Manson Icefield since the last deglaciation. The results of this study yield the following generalizations and conclusions:

- Quartz-, feldspar- and sand-rich laminated glacial sediments (prior to ~11 cal. ka BP) in core 01PC were probably deposited by subglacial hyperpycnal currents triggered by the local dynamic of the southern margin of the IIS from Cape Norton Shaw Inlet.
- Mineralogical, physical and geochemical signatures of deglacial sediments support the hypothesis of the deglaciation of eastern Smith and Jones sounds at 11 to 10.7 cal. ka BP and approximately 10.7 cal. ka BP, respectively. The increase in reddish clays/fine silt of the Thule Supergroup during the Early Holocene may indicate the implementation of the formation of cyclonic circulation of the WGC in the NOW at ~10.8 cal. ka BP.
- Following the opening of Nares Strait (~8.3 cal. ka BP), high levels of carbonate-rich IRD export from Nares Strait to northern Baffin Bay take place until 6.6 cal. ka BP, typifying the establishment of the modern Arctic–Atlantic throughflow. After 6.6 cal. ka BP, the sediment provenance in the inlet is mainly dominated by Canadian Shield sources, indicating that sedimentation is mainly influenced by Cape Norton Shaw glacier discharges.
- The lower sedimentation rate (~6 cm ka^{-1}) recorded between 6.6 and 2 cal. ka BP in core 01PC indicates that warmer marine conditions prevalent in northern Baffin Bay at this time induced an accelerated landward retreat of the Cape Norton Shaw glaciers.
- Variations in the glaciogenic sediment inputs and sea-ice rafting in Cape Norton Shaw Inlet have a strong overprint on the $\overline{SS}$ record in cores 01PC and 02BC. Thus, our results suggest that careful attention must be paid when interpreting sortable silt data as a proxy for past bottom current speed in glacier-proximal settings.
- Grain-size data in core 02BC reveal that colder conditions associated with the LIA period promoted glacier growth and increased iceberg calving activity and sea-ice export through Cape Norton Shaw Inlet.
- The similar increasing trend observed in (Bt + Chl)/Pl and fine-grained sediments from core 02BC and the Arctic surface air anomaly since the industrial period (~1800 CE to present) supports the idea that increased atmospheric temperatures have had an important influence on the dynamics of Cape Norton Shaw glaciers since the end of the LIA.

Overall, the multiproxy approach presented in this study has allowed us to refine knowledge concerning the evolution of sediment dynamics in northwestern Baffin Bay since the last deglaciation and provided a better understanding of the response of the Cape Norton Shaw glaciers to changing climate and oceanographic conditions of the Holocene.

Acknowledgments. – We are grateful to the captain, officers, crew and scientists onboard the CCGS *Amundsen* during the 2018 (Leg 3) ArcticNet expedition for the recovery of the sediment cores used in this study. We also thank Quentin Beauvais (ISMER-UQAR), Maria-Emilia Rodriguez-Cuicas (ISMER-UQAR), Marie Girieud (ISMER-UQAR), Nicolas Van Nieuwenhove (University of New Brunswick), Marie-Claire Perello (Université de Bordeaux) and Margaux Saint George (Université de Bordeaux) for their technical support and advice in the laboratory. The authors declare that they have no conflicts of interest. Last, we thank Kelly Hogan and John T. Andrews for their constructive reviews, which helped to improve the quality of the manuscript, as well as to Jan A. Piotrowski for his editorial work. This research was funded by ArcticNet (a Network of Centers of Excellence Canada), Québec-Océan, GEOTOP and the Natural Sciences and Engineering Research Council of Canada (NSERC) through discovery grants to J.-C. Montero-Serrano and G. St-Onge.

Author contributions. – NS performed the grain-size analysis, ran the statistical analyses on the grain-size data, made the Bayesian age model, wrote the original draft of the manuscript and made the figures. JCMS led the project, acquired the funds for core sampling and analysis, performed the qXRD analysis, ran the statistical analyses on the qXRD and pXRF data and acquired the radiocarbon dates. FE co-led the project and supervised the grain-size analysis and the preparation of thin sections. GSO supervised the physical and elemental geochemical analysis of sediment cores. SZ co-supervised the preparation of thin sections. LC assisted with editing and reviewing the manuscript. All authors contributed to reviewing and editing the manuscript.

Data availability statement. – All analytical data presented are available electronically in the PANGAEA database (https://doi.pangaea.de/10.1594/PANGAEA.932231).

References

Aagaard, K. & Carmack, E. C. 1989: The role of sea ice and other fresh water in the Arctic circulation. *Journal of Geophysical Research 94*, 14485, https://doi.org/10.1029/JC094iC10p14485.

Andrews, J. T. 2000: Icebergs and Iceberg Rafted Detritus (IRD) in the North Atlantic: facts and assumptions. *Oceanography 13*, 100–108.

Andrews, J. T. 2019: Baffin Bay/Nares Strait surface (seafloor) sediment mineralogy: further investigations and methods to elucidate spatial variations in provenance. *Canadian Journal of Earth Sciences 56*, 814–828.

Andrews, J. T. & Eberl, D. D. 2011: Surface (sea floor) and near-surface (box cores) sediment mineralogy in Baffin Bay as a key to sediment provenance and ice sheet variations. *Canadian Journal of Earth Sciences 48*, 1307–1328.

Andrews, J. T. & Eberl, D. D. 2012: Determination of sediment provenance by unmixing the mineralogy of source-area sediments: the 'SedUnMix' program. *Marine Geology 291–294*, 24–33.

Andrews, J. T., Bjork, A. A., Eberl, D. D., Jennings, A. E. & Verplanck, E. P. 2015: Significant differences in late Quaternary bedrock erosion and transport: east versus West Greenland ~70°N - evidence from the mineralogy of offshore glacial marine sediments. *Journal of Quaternary Science 30*, 452–463.

Andrews, J. T., Klein, A. J., Jenner, K. A., Jennings, A. E. & Campbell, C. 2018: The variability of Baffin Bay seafloor sediment mineralogy: the identification of discrete glacial sediment sources and application to Late Quaternary downcore analysis. *Canadian Journal of Earth Sciences 55*, 620–639.

Bailey, J. N. L., Macdonald, R. W., Sanei, H., Outridge, P. M., Johannessen, S. C., Hochheim, K., Barber, D. & Stern, G. A. 2013: Change at the margin of the North Water Polynya, Baffin Bay, inferred from organic matter records in dated sediment cores. *Marine Geology 341*, 1–13.

Berger, A. & Loutre, M. F. 1991: Insolation values for the climate of the last 10 million years. *Quaternary Science Reviews 10*, 297–317.

Blake, J. W. 1981: Neoglacial fluctuations of glaciers, southeastern Ellesmere Island, Canadian Arctic Archipelago. *Geografiska Annaler. Series A, Physical Geography 63*, 201–218.

Blake, J. W. 1992: Shell-bearing till along Smith Sound, Ellesmere Island - Greenland: age and significance. *Sveriges Geologiska Undersökning 81*, 51–58.

Blake, J. W. 1993: Holocene emergence along the Ellesmere Island coasts of northernmost Baffin Bay. *Norsk Geologisk Tidsskrift 73*, 147–160.

Blake, J. W., Jackson, H. R. & Currie, C. G. 1996: Seafloor evidence for glaciation, northernmost Baffin Bay. *Bulletin of the Geological Society of Denmark 43*, 157–168.

Bradley, R. S. 2003: Climate change: climate in medieval time. *Science 302*, 404–405.

Brossard, J. 2021: *Dynamique sédimentaire holocène dans le détroit de Jones reconstituée à partir des carottes sédimentaires recueillies dans la baie de Belcher (calotte glaciaire de Devon, Nunavut, Canada)*. Mémoire. Rimouski, Québec, Université du Québec à Rimouski, Institut des sciences de la mer de Rimouski (ISMER), 116 pp.

Caron, M., Montero-Serrano, J. C., St-Onge, G. & Rochon, A. 2020: Quantifying provenance and transport pathways of Holocene sediments from the Northwestern Greenland margin. *Paleoceanography and Paleoclimatology 35*, e2019PA003809, https://doi.org/10.1029/2019PA003809.

Caron, M., Rochon, A., Montero-Serrano, J. C. & St-Onge, G. 2019: Evolution of sea-surface conditions on the northwestern Greenland margin during the Holocene. *Journal of Quaternary Science 34*, 569–580.

Chauché, N., Hubbard, A., Gascard, J. C., Box, J. E., Bates, R., Koppes, M., Sole, A., Christoffersen, P. & Patton, H. 2014: Ice–ocean interaction and calving front morphology at two west Greenland tidewater outlet glaciers. *The Cryosphere 8*, 1457–1468.

Ciracì, E., Velicogna, I. & Swenson, S. 2020: Continuity of the mass loss of the world's glaciers and ice caps from the GRACE and GRACE Follow-On missions. *Geophysical Research Letters 47*, e2019GL086926, https://doi.org/10.1029/2019GL086926.

Cook, A. J., Copland, L., Noël, B. P. Y., Stokes, C. R., Bentley, M. J., Sharp, M. J., Bingham, R. G. & van den Broeke, M. R. 2019: Atmospheric forcing of rapid marine-terminating glacier retreat in the Canadian Arctic Archipelago. *Science Advances 5*, eaau8507, https://doi.org/10.1126/sciadv.aau8507.

Copland, L., Sharp, M. J. & Dowdeswell, J. A. 2003: The distribution and flow characteristics of surge-type glaciers in the Canadian High Arctic. *Annals of Glaciology 36*, 73–81.

Cormier, M. A., Rochon, A., de Vernal, A. & Gélinas, Y. 2016: Multiproxy study of primary production and paleoceanographical conditions in Northern Baffin Bay during the last centuries. *Marine Micropaleontology 127*, 1–10.

Coulthard, R. D., Furze, M. F. A., Pieńkowski, A. J., Chantel Nixon, F. & England, J. H. 2010: New marine ΔR values for Arctic Canada. *Quaternary Geochronology 5*, 419–434.

Croudace, I. W. & Rothwell, R. G. 2015: *Micro-XRF Studies of Sediment Cores: Applications of a Non-Destructive Tool for the Environmental Sciences*. 421 pp. Springer, Dordrecht.

Curley, A., Kochtitzky, W., Edwards, B. & Copland, L. 2021: Glacier changes over the past 144 years at Alexandra Fiord, Ellesmere Island, Canada. *Journal of Glaciology 67*, 511–522.

Curry, R. & Mauritzen, C. 2005: Dilution of the Northern North Atlantic Ocean in Recent Decades. *Science 308*, 1772–1774.

Dalton, A. S. and 70 others 2020: An updated radiocarbon-based ice margin chronology for the last deglaciation of the North American Ice Sheet complex. *Quaternary Science Reviews 234*, 106223, https://doi.org/10.1016/j.quascirev.2020.106223.

Darby, D. A. 2003: Sources of sediment found in sea ice from the western Arctic Ocean, new insights into processes of entrainment and drift patterns. *Journal of Geophysical Research 108*, 3257, https://doi.org/10.1029/2002JC001350.

Deschamps, C. E., Montero-Serrano, J. C. & St-Onge, G. 2018: Sediment provenance changes in the Western Arctic Ocean in response to ice rafting, sea level, and oceanic circulation variations since the last deglaciation. *Geochemistry, Geophysics, Geosystems 19*, 2147–2165.

Dickson, R., Rudels, B., Dye, S., Karcher, M., Meincke, J. & Yashayaev, I. 2007: Current estimates of freshwater flux through Arctic and subarctic seas. *Progress in Oceanography 73*, 210–230.

Dowdeswell, J. A. & Cromack, M. 1991: Behaviour of a glacier-derived suspended sediment plume in a small Arctic inlet. *Journal of Geology 99*, 111–123.

Dowdeswell, J. A., Hogan, K. A., Arnold, N. S., Mugford, R. I., Wells, M., Hirst, J. P. P. & Decalf, C. 2015: Sediment-rich meltwater plumes and ice-proximal fans at the margins of modern and ancient tidewater glaciers: observations and modelling. *Sedimentology 62*, 1665–1692.

Dyke, A. S. 1998: Holocene delevelling of Devon Island, Arctic Canada: implications for ice sheet geometry and crustal response. *Canadian Journal of Earth Sciences 35*, 885–904.

Dyke, A. S., Andrews, J. T., Clark, P. U., England, J. H., Miller, G. H., Shaw, J. & Veillette, J. J. 2002: The Laurentide and Innuitian Ice Sheets during the Last Glacial Maximum. *Quaternary Science Reviews 21*, 9–31.

Dyke, A. S. & Evans, D. J. A. 2003: Ice-marginal terrestrial landsystems: Northern Laurentide and Innuitian Ice Sheet margins. *Glacial Landsystems 24*, 143–165.

Dyke, A. S., Hooper, J., Harington, C. R. & Savelle, J. M. 1999: The late wisconsinan and Holocene record of walrus (*Odobenus rosmarus*) from North America: a review with new data from Arctic and Atlantic Canada. *Arctic 52*, 160–181.

Dyke, A. S., Savelle, J. M., Szpak, P., Southon, J. R., Howse, L., Desrosiers, P. M. & Kotar, K. 2019: An assessment of marine reservoir corrections for radiocarbon dates on walrus from the Foxe basin region of Arctic Canada. *Radiocarbon 61*, 67–81.

Eberl, D. D. 2003: User Guide to RockJock – A program for determining quantitative mineralogy from X-ray diffraction data. *U.S. Geological Survey, Open-File Report 2003-78*, 47 pp.

England, J. H., Atkinson, N., Bednarski, J., Dyke, A. S., Hodgson, D. A., & Ó Cofaigh, C. 2006: The Innuitian Ice Sheet: configuration, dynamics and chronology. *Quaternary Science Reviews 25*, 689–703.

von Eynatten, H., Barcelo-Vidal, C. & Pawlowsky-Glahn, V. 2003: Composition and Discrimination of sandstones: a statistical evaluation of different analytical methods. *Journal of Sedimentary Research 73*, 47–57.

Furze, M. F. A., Pieńkowski, A. J., McNeely, M. A., Bennett, R. & Cage, A. G. 2017: Deglaciation and ice shelf development at the northeast margin of the Laurentide Ice Sheet during the Younger Dryas chronozone. *Boreas 47*, 271–296.

Gamboa, A., Montero-Serrano, J.-C., St-Onge, G., Rochon, A. & Desiage, P. A. 2017: Mineralogical, geochemical, and magnetic signatures of surface sediments from the Canadian Beaufort Shelf and Amundsen Gulf (Canadian Arctic): Canadian beaufort shelf and Amundsen Gulf. *Geochemistry, Geophysics, Geosystems 18*, 488–512.

Georgiadis, E., Giraudeau, J., Martinez, P., Lajeunesse, P., St-Onge, G., Schmidt, S. & Massé, G. 2018: Deglacial to postglacial history of Nares Strait, Northwest Greenland: a marine perspective from Kane Basin. *Climate of the Past 14*, 1991–2010.

Gilbert, R. 1982: Contemporary sedimentary environments on Baffin Island, N.W.T., Canada: glaciomarine processes in Fiords of Eastern Cumberland Peninsula. *Arctic and Alpine Research 14*, 1–12.

Grobe, H. 1987: A simple method for the determination of ice-rafted debris in sediment cores. *Polarforschung 57*, 123–126.

Hansen, K. E., Giraudeau, J., Wacker, L., Pearce, C. & Seidenkrantz, M.-S. 2020: Reconstruction of Holocene oceanographic conditions in Eastern Baffin Bay. *Climate of the Past 16*, 1075–1095.

Harrison, J. C., St-Onge, M. R., Petrov, O., Strelnikov, S., Lopatin, B., Wilson, F., Tella, S., Paul, D., Lynds, T., Shokalsky, S., Hults, C., Bergman, S., Jepsen, H. F. & Solli, A. 2011: Geological map of the Arctic. *Geological Survey of Canada, 'A' Series Map 2159A, scale 1:5 000 000*.

Heaton, T. J., Köhler, P., Butzin, M., Bard, E., Reimer, R. W., Austin, W. E. N., Bronk Ramsey, C., Grootes, P. M., Hughen, K. A., Kromer, B., Reimer, P. J., Adkins, J., Burke, A., Cook, M. S., Olsen, J. & Skinner, L. C. 2020: Marine20—the marine radiocarbon age calibration curve (0–55,000 cal BP). *Radiocarbon 62*, 779–820.

Hodgson, D. A. 1985: The last glaciation of west-central Ellesmere Island, Arctic Archipelago, Canada. *Canadian Journal of Earth Sciences 22*, 347–368.

Hodson, D. L. R., Keeley, S. P. E., West, A., Ridley, J., Hawkins, E. & Hewitt, H. T. 2013: Identifying uncertainties in Arctic climate change projections. *Climate Dynamics 40*, 2849–2865.

Hogan, K. A., Jakobsson, M., Mayer, L., Reilly, B. T., Jennings, A. E., Stoner, J. S., Nielsen, T., Andresen, K. J., Nørmark, E., Heirman, K. A., Kamla, E., Jerram, K., Stranne, C. & Mix, A. 2020: Glacial sedimentation, fluxes and erosion rates associated with ice retreat in Petermann Fjord and Nares Strait, north-west Greenland. *The Cryosphere 14*, 261–286.

Holland, M. M., Bitz, C. M., Eby, M. & Weaver, A. J. 2001: The role of ice–ocean interactions in the variability of the North Atlantic thermohaline circulation. *Journal of Climate 14*, 656–675.

Hua, Q. 2009: Radiocarbon: A chronological tool for the recent past. *Quaternary Geochronology 4*, 378–390.

Jaccard, S. L., Galbraith, E. D., Sigman, D. M., Haug, G. H., Francois, R., Pedersen, T. F., Dulski, P. & Thierstein, H. R. 2009: Subarctic Pacific evidence for a glacial deepening of the oceanic respired carbon pool. *Earth and Planetary Science Letters 277*, 156–165.

Jackson, R., Kvorning, A. B., Limoges, A., Georgiadis, E., Olsen, S. M., Tallberg, P., Andersen, T. J., Mikkelsen, N., Giraudeau, J., Massé, G., Wacker, L. & Ribeiro, S. 2021: Holocene polynya dynamics and their interaction with oceanic heat transport in northernmost Baffin Bay. *Scientific Reports 11*, 10095, https://doi.org/10.1038/s41598-021-88517-9.

Jakobsson, M., Hogan, K. A., Mayer, L. A., Mix, A., Jennings, A., Stoner, J., Eriksson, B., Jerram, K., Mohammad, R., Pearce, C., Reilly, B. & Stranne, C. 2018: The Holocene retreat dynamics and stability of Petermann Glacier in northwest Greenland. *Nature Communications 9*, 2104, https://doi.org/10.1038/s41467-018-04573-2.

Jennings, A. E., Andrews, J. T., Oliver, B., Walczak, M. & Mix, A. 2019: Retreat of the smith sound ice stream in the early Holocene. *Boreas 48*, 825–840.

Jennings, A. E., Sheldon, C., Cronin, T., Francus, P., Stoner, J. & Andrews, J. 2011: The Holocene History of Nares Strait: transition from glacial bay to Arctic–Atlantic throughflow. *Oceanography 24*, 26–41.

Jones, P. D. & Mann, M. E. 2004: Climate over past millennia. *Review of Geophysics 42*, RG2002, https://doi.org/10.1029/2003RG000143.

Jones, E. P., Swift, J. H., Anderson, L. G., Lipizer, M., Civitarese, G., Falkner, K. K., Kattner, G. & McLaughlin, F. 2003: Tracing Pacific water in the North Atlantic Ocean. *Journal of Geophysical Research 108*, 3116, https://doi.org/10.1029/2001JC001141.

Kaplan, M. R. & Wolfe, A. P. 2006: Spatial and temporal variability of Holocene temperature in the North Atlantic region. *Quaternary Research 65*, 223–231.

Kaufman, D. S., Schneider, D. P., McKay, N. P., Ammann, C. M., Bradley, R. S., Briffa, K. R., Miller, G. H., Otto-Bliesner, B. L., Overpeck, J. T., Vinther, B. M. & Arctic Lakes 2k Project Members 2009: Recent warming reverses long-term Arctic cooling. *Science 325*, 1236–1239.

Koerner, K. A., Limoges, A., Van Nieuwenhove, N., Richerol, T., Massé, M. & Ribeiro, S. 2021: Late Holocene sea-surface changes in the North Water polynya reveal freshening of northern Baffin Bay in the 21st century. *Global and Planetary Change 206*, 103642, https://doi.org/10.1016/j.gloplacha.2021.103642.

Lacourse, T. & Gajewski, K. 2020: Current practices in building and reporting age–depth models. *Quaternary Research 96*, 28–38.

Laskar, J., Robutel, P., Joutel, F., Gastineau, M., Correia, A. C. M. & Levrard, B. 2004: A long-term numerical solution for the insolation quantities of the Earth. *Astronomy & Astrophysics 428*, 261–285.

Lecavalier, B. S., Fisher, D. A., Milne, G. A., Vinther, B. M., Tarasov, L., Huybrechts, P., Lacelle, D., Main, B., Zheng, J., Bourgeois, J. & Dyke, A. S. 2017: High Arctic Holocene temperature record from the Agassiz ice cap and Greenland ice sheet evolution. *PNAS 114*, 5952–5957.

Ledu, D., Rochon, A., de Vernal, A. & St-Onge, G. 2010: Holocene paleoceanography of the northwest passage, Canadian Arctic Archipelago. *Quaternary Science Reviews 29*, 3468–3488.

Lenaerts, J. T. M., van Angelen, J. H., van den Broeke, M. R., Gardner, A. S., Wouters, B. & van Meijgaard, E. 2013: Irreversible mass loss of Canadian Arctic Archipelago glaciers. *Geophysical Research Letters 40*, 870–874.

Letaïef, S., Montero-Serrano, J.-C. & St-Onge, G. 2021: Sedimentary processes within the Canadian Arctic Archipelago: Relationships among sedimentological, geochemical, and magnetic sediment properties. *Geochemistry, Geophysics, Geosystems 22*, e2021GC009719, https://doi.org/10.1029/2021GC009719.

Lougheed, B. C. & Obrochta, S. P. 2019: A rapid, deterministic age–depth modeling routine for geological sequences with inherent depth uncertainty. *Paleoceanography and Paleoclimatology 34*, 122–133.

Macdonald, R. W. & Gobeil, C. 2012: Manganese sources and sinks in the Arctic Ocean with reference to periodic enrichments in Basin sediments. *Aquatic Geochemistry 18*, 565–591.

McCave, I. N. & Andrews, J. T. 2019a: Distinguishing current effects in sediments delivered to the ocean by ice. I. Principles, methods and examples. *Quaternary Science Reviews 212*, 92–107.

McCave, I. N. & Andrews, J. T. 2019b: Distinguishing current effects in sediments delivered to the ocean by ice. II. Glacial to Holocene changes in high latitude North Atlantic upper ocean flows. *Quaternary Science Reviews 223*, 105902, https://doi.org/10.1016/j.quascirev.2019.105902.

McCave, I. N., Manighettia, B. & Robinson, S. G. 1995: Sortable silt and fine sediment size/composition slicing: parameters for palaeocurrent speed and palaeoceanography. *Paleoceanography and Paleoclimatology 10*, 593–610, https://doi.org/10.1029/94PA03039.

McNeely, R., Dyke, A. S. & Southon, J. R. 2006: Canadian Marine Reservoir Ages, Preliminary Data Assessment. *Geological Survey of Canada, Open File 5049*, 3 pp.

Millan, R., Mouginot, J. & Rignot, E. 2017: Mass budget of the glaciers and ice caps of the Queen Elizabeth Islands, Canada, from 1991 to 2015. *Environmental Research Letters 12*, 024016, https://doi.org/10.1088/1748-9326/aa5b04.

Montero-Serrano, J. C., Brossard, J. & Corminboeuf, A. 2018: *Collecting Sedimentary Sequences for Paleoclimate, Paleoceanographic and Environmental Studies in the Eastern Canadian Arctic*

Archipelago and Baffin Bay. ArcticNet Leg 3 Cruise Report - CCGS Amundsen. CCGS, Australia, 14 pp.
Montero-Serrano, J. C., Föllmi, K. B., Adatte, T., Spangenberg, J. E., Tribovillard, N., Fantasia, A. & Suan, G. 2015: Continental weathering and redox conditions during the early Toarcian Oceanic Anoxic Event in the northwestern Tethys: insight from the Posidonia Shale section in the Swiss Jura Mountains. *Palaeogeography, Palaeoclimatology, Palaeoecology 429*, 83–99.
Montero-Serrano, J. C., Palarea-Albaladejo, J., Martín-Fernández, J. A., Martínez-Santana, M. & Gutiérrez-Martín, J. V. 2010: Sedimentary chemofacies characterization by means of multivariate analysis. *Sedimentary Geology 228*, 218–228.
Mortimer, C. A. & Sharp, M. 2018: Spatiotemporal variability of Canadian High Arctic glacier surface albedo from MODIS data, 2001–2016. *The Cryosphere 12*, 701–720.
Mouret, A., Anschutz, P., Lecroart, P., Chaillou, G., Hyacinthe, C., Deborde, J., Jorissen, F. J., Deflandre, B., Schmidt, S. & Jouanneau, J. M. 2009: Benthic geochemistry of manganese in the Bay of Biscay, and sediment mass accumulation rate. *Geo-Marine Letters 29*, 133–149.
Mudie, P. J., Rochon, A., Prins, M. A., Soenarjo, D., Troelstra, S. R., Levac, E., Scott, D. B., Roncaglia, L. & Kuijpers, A. 2006: Late pleistocene-Holocene marine geology of Nares strait region: palaeoceanography from Foraminifera and Dinoflagellate cysts, Sedimentology and Stable Isotopes. *Polarforschung 74*, 169–183.
Mulder, T., Syvitski, J. P., Migeon, S., Faugeres, J. C. & Savoye, B. 2003: Marine hyperpycnal flows: initiation, behavior and related deposits. *Marine and Petroleum Geology 20*, 861–882.
Noël, B., van de Berg, W. J., Lhermitte, S., Wouters, B., Schaffer, N. & van den Broeke, M. R. 2018: Six decades of glacial mass loss in the Canadian Arctic archipelago. *Journal of Geophysical Research: Earth Surface 123*, 1430–1449.
Nürnberg, D., Wollenburg, J., Dethleff, D., Eicken, H., Kassens, H., Letzig, T., Reimnitz, E. & Thiede, J. 1994: Sediments in Arctic sea ice: implications for entrainment transport and release. *Marine Geology 119*, 184–214.
Ó Cofaigh, C., Andrews, J. T., Jennings, A. E., Dowdeswell, J. A., Hogan, K. A., Kilfeather, A. A. & Sheldon, C. 2013: Glacimarine lithofacies, provenance and depositional processes on a West Greenland trough-mouth fan. *Journal of Quaternary Science 28*, 13–26.
Ó Cofaigh, C. & Dowdeswell, J. A. 2001: Laminated sediments in glacimarine environments: diagnostic criteria for their interpretation. *Quaternary Science Reviews 20*, 1411–1436.
O'Regan, M., Sellén, E. & Jakobsson, M. 2014: Middle to late Quaternary grain size variations and sea-ice rafting on the Lomonosov Ridge. *Polar Research 33*, 23672, https://doi.org/10.3402/polar.v33.23672.
Pieńkowski, A. J., England, J. H., Furze, M. F. A., Blasco, S., Mudie, P. J. & MacLean, B. 2013: 11,000 yrs of environmental change in the Northwest passage: a multiproxy core record from central Parry Channel, Canadian High Arctic. *Marine Geology 341*, 68–85.
Pieńkowski, A. J., England, J. H., Furze, M. F. A., Marret, F., Eynaud, F., Vilks, G., Maclean, B., Blasco, S. & Scourse, J. D. 2012: The deglacial to postglacial marine environments of SEBarrow Strait, Canadian Arctic Archipelago. *Boreas 41*, 141–179.
Poulton, S. W. & Raiswell, R. 2005: Chemical and physical characteristics of iron oxides in riverine and glacial meltwater sediments. *Chemical Geology 218*, 203–221.
Powell, R. D. 1981: A model for sedimentation by tidewater glaciers. *Annals of Glaciology 2*, 129–134.
Reilly, B. T., Stoner, J. S., Mix, A. C., Walczak, M. H., Jennings, A., Jakobsson, M., Dyke, L., Glueder, A., Nicholls, K., Hogan, K. A., Mayer, L. A., Hatfield, R. G., Albert, S., Marcott, S., Fallon, S. & Cheseby, M. 2019: Holocene break-up and reestablishment of the Petermann Ice Tongue, Northwest Greenland. *Quaternary Science Reviews 218*, 322–342.
Reimnitz, E., Kempema, E. W. & Barnes, P. W. 1987: Anchor ice, seabed freezing, and sediment dynamics in shallow Arctic seas. *Journal of Geophysical Research-Oceans 92*, 14671–14678.
Reimnitz, E., McCormick, M., McDougall, K. & Brouwers, E. 1993: Sediment export by ice rafting from a coastal polynya, Arctic Alaska, U.S.A. *Arctic and Alpine Research 25*, 83–98.
Ribeiro, S., Limoges, A., Massé, G., Johansen, K. L., Colgan, W., Weckström, K., Jackson, R., Georgiadis, E., Mikkelsen, N., Kuijpers, A., Olsen, J., Olsen, S. M., Nissen, M., Andersen, T. J., Strunk, A., Wetterich, S., Syväranta, J., Henderson, A. C. G., Mackay, H., Taipale, S., Jeppesen, E., Larsen, N. K., Crosta, X., Giraudeau, J., Wengrat, S., Nuttall, M., Grønnow, B., Mosbech, A. & Davidson, T. A. 2021: Vulnerability of the North Water ecosystem to climate change. *Nature Communications 12*, 4475, https://doi.org/10.1038/s41467-021-24742-0.
Rochon, A. & de Vernal, A. 1994: Palynomorph distribution in recent sediments from the Labrador Sea. *Canadian Journal of Earth Sciences 31*, 115–127.
Rykova, T., Straneo, F. & Bower, A. S. 2015: Seasonal and interannual variability of the West Greenland current system in the Labrador sea in 1993–2008. *Journal of Geophysical Research: Oceans 120*, 1318–1332.
Sharp, M., Burgess, D. O., Cawkwell, F., Copland, L., Davis, J. A., Dowdeswell, E. K., Dowdeswell, J. A., Gardner, A. S., Mair, D., Wang, L., Williamson, S. N., Wolken, G. J. & Wyatt, F. 2014: Remote sensing of recent glacier changes in the Canadian Arctic. *In* Kargel, J. S., Leonard, G. J., Bishop, M. P., Kääb, A. & Raup, B. H. (eds.): *Global Land Ice Measurements from Space*, Chapter 9, 205–228. Springer Praxis Books, Springer, Berlin, Heidelberg.
Solomina, O. N., Bradley, R. S., Hodgson, D. A., Ivy-Ochs, S., Jomelli, V., Mackintosh, A. N., Nesje, A., Owen, L. A., Wanner, H., Wiles, G. C. & Young, N. E. 2015: Holocene glacier fluctuations. *Quaternary Science Reviews 111*, 9–34.
Spielhagen, R. F., Werner, K., Sørensen, S. A., Zamelczyk, K., Kandiano, E., Budeus, G., Husum, K., Marchitto, T. M. & Hald, M. 2011: Enhanced modern heat transfer to the Arctic by warm Atlantic water. *Science 331*, 450–453.
Spofforth, D. J. A., Pälike, H. & Green, D. 2008: Paleogene record of elemental concentrations in sediments from the Arctic Ocean obtained by XRF analyses: paleogene XRF data from the Arctic Ocean. *Paleoceanography 23*, PA1S09, https://doi.org/10.1029/2007PA001489.
Stokes, C. R., Tarasov, L., Blomdin, R., Cronin, T. M., Fisher, T. G., Gyllencreutz, R., Hättestrand, C., Heyman, J., Hindmarsh, R. C. A., Hughes, A. L. C., Jakobsson, M., Kirchner, N., Livingstone, S. J., Margold, M., Murton, J. B., Noormets, R., Peltier, W. R., Peteet, D. M., Piper, D. J. W., Preusser, F., Renssen, H., Roberts, D. H., Roche, D. M., Saint-Ange, F., Stroeven, A. P. & Teller, J. T. 2015: On the reconstruction of Palaeo-Ice Sheets: recent advances and future challenges. *Quaternary Science Reviews 125*, 15–49.
St-Onge, M. P. & St-Onge, G. 2014: Environmental changes in Baffin Bay during the Holocene based on the physical and magnetic properties of sediment cores: environmental changes in Baffin bay during the Holocene. *Journal of Quaternary Science 29*, 41–56.
Stuiver, M., Reimer, P. J. & Reimer, R. W. 2017: *CALIB 7.1*. Available online at: http://calib.org/calib/calib.html.
Tang, C. C. L., Ross, C. K., Yao, T., Petrie, B., DeTracey, B. M. & Dunlap, E. 2004: The circulation, water masses and sea-ice of Baffin Bay. *Progress in Oceanography 63*, 183–228.
Telford, R. J., Heegaard, E. & Birks, H. J. B. 2004: All age–depth models are wrong: but how badly? *Quaternary Science Reviews 23*, 1–5.
Thomas, E. K., Szymanski, J. & Briner, J. P. 2010: Holocene alpine glaciation inferred from lacustrine sediments on northeastern Baffin Island, Arctic Canada: Baffin Island Holocene glaciation inferred from lacustrine sediments. *Journal of Quaternary Science 25*, 146–161.
Thomson, L. I., Osinski, G. R. & Ommanney, S. L. 2011: Glacier change on Axel Heiberg Island, Nunavut, Canada. *Journal of Glaciology 57*, 1079–1086.
Toucanne, S., Soulet, G., Vázquez Riveiros, N., Boswell, S. M., Dennielou, B., Waelbroeck, C., Bayon, G., Mojtahid, M., Bosq, M., Sabine, M., Zaragosi, S., Bourillet, J. F. & Mercier, H. 2021: The North Atlantic Glacial Eastern Boundary Current as a Key Driver for Ice-Sheet—AMOC Interactions and Climate Instability. *Paleoceanography and Paleoclimatology 36*, e2020PA004068, https://doi.org/10.1029/2020PA004068.
Trachsel, M. & Telford, R. J. 2017: All age–depth models are wrong, but are getting better. *The Holocene 27*, 860–869.

Tremblay, J. É. 2002: Impact of the large-scale Arctic circulation and the North Water Polynya on nutrient inventories in Baffin Bay. *Journal of Geophysical Research 107*, 3112, https://doi.org/10.1029/2000JC000595.

Van Wychen, W., Burgess, D. O., Gray, L., Copland, L., Sharp, M., Dowdeswell, J. A. & Benham, T. J. 2014: Glacier velocities and dynamic ice discharge from the Queen Elizabeth Islands, Nunavut, Canada: Glacier velocities and ion flux, QEI. *Geophysical Research Letters 41*, 484–490.

Van Wychen, W., Copland, L. & Burgess, D. 2020: Ice masses of the eastern Canadian arctic archipelago. *In* Slaymaker, O. & Catto, N. (eds.): *Landscapes and Landforms of Eastern Canada*, 297–314. Springer International Publishing, Cham.

Van Wychen, W., Davis, J., Burgess, D. O., Copland, L., Gray, L., Sharp, M. & Mortimer, C. 2016: Characterizing interannual variability of glacier dynamics and dynamic discharge (1999–2015) for the ice masses of Ellesmere and Axel Heiberg Islands, Nunavut, Canada: Glacier dynamics of the Canadian arctic. *Journal of Geophysical Research: Earth Surface 121*, 39–63.

Waelbroeck, C. and 62 others 2019: Consistently dated Atlantic sediment cores over the last 40 thousand years. *Scientific Data 6*, 165, https://doi.org/10.1038/s41597-019-0173-8.

Wagner, T. J. W., Straneo, F., Richards, C. G., Slater, D. A., Stevens, L. A., Das, S. B. & Singh, H. 2019: Large spatial variations in the flux balance along the front of a Greenland tidewater glacier. *The Cryosphere 13*, 911–925.

Walker, M. J. C., Berkelhammer, M., Björck, S., Cwynar, L. C., Fisher, D. A., Long, A. J., Lowe, J. J., Newnham, R. M., Rasmussen, S. O. & Weiss, H. 2012: Formal subdivision of the Holocene series/epoch: a discussion paper by a working group of INTIMATE (integration of ice-core, marine and terrestrial records) and the subcommission on quaternary stratigraphy (international commission on stratigraphy). *Journal of Quaternary Science 27*, 649–659.

Weiser, J., Titschack, J., Kienast, M., McCave, I. N., Lochte, A. A., Saini, J., Stein, R. & Hebbeln, D. 2021: Atlantic water inflow to Labrador Sea and its interaction with ice sheet dynamics during the Holocene. *Quaternary Science Reviews 256*, 106833, https://doi.org/10.1016/j.quascirev.2021.106833.

Weltje, G. J. & Tjallingii, R. 2008: Calibration of XRF core scanners for quantitative geochemical logging of sediment cores: Theory and application. *Earth and Planetary Science Letters 274*, 423–438.

White, A. & Copland, L. 2018: Area changes of glaciers across Northern Ellesmere Island, Nunavut, between ~1999 and ~2015. *Journal of Glaciology 64*, 609–623.

Wu, L., Wilson, D. J., Wang, R., Yin, X., Chen, Z., Xiao, W. & Huang, M. 2020: Evaluating Zr/Rb ratio from XRF scanning as an indicator of grain-size variations of glaciomarine sediments in the Southern Ocean. *Geochemistry, Geophysics, Geosystems 21*, e2020GC009350, https://doi.org/10.1029/2020GC009350.

Zaragosi, S., Bourillet, J. F., Eynaud, F., Toucanne, S., Denhard, B., Van Toer, A. & Lanfumey, V. 2006: The impact of the last European deglaciation on the deep-sea turbidite systems of the Celtic-Armorican margin (Bay of Biscay). *Geo-Marine Letters 26*, 317–329.

Zweng, M. M. & Münchow, A. 2006: Warming and freshening of Baffin Bay, 1916–2003. *Journal of Geophysical Research 111*, C07016, https://doi.org/10.1029/2005JC003093.

Supporting Information

Additional Supporting Information may be found in the online version of this article at http://www.boreas.dk.

Fig S1. Core top correlations of cores 01PC and 02BC with the help of physical parameters: magnetic susceptibility, colour reflectance parameter a^* and density.

Fig S2. Stratigraphical distributions of mineralogical (A) and geochemical (B) data of cores 01PC and 02BC. Grey lines are for core 02BC and black lines are for core 01PC.

Fig S3. A. Scatter plot of Fe/Al and Mn/Al. The black line is the tendency curve with the coefficient of determination r^2. B. Scatter plot of $\overline{SS}$ (μm) and SS% (note that all of the data sets show a coefficient of correlation of $r = 0.95$). C. Scatter plot of $\overline{SS}$ (μm) and fine (63–250 μm) sand (%). D. Scatter plot of SS% and fine (63–250 μm) sand (%). E and F. Downcore runs (5 points) for correlation (correl 5) and slope (slope 5) for cores 01PC (E) and 02BC (F) (see McCave & Andrews 2019a for more details).

Fig S4. Photography of the >125 μm fraction from Unit 1 (right), Unit 2 (middle) and Unit 3 (left).

Data S1. Analytical procedure.

Data S2. Statistical approach and sediment unmixing model.